Remote Sensing of Environment 311 (2024) 114302

Contents lists available at ScienceDirect

Remote Sensing of Environment

journal homepage: www.elsevier.com/locate/rse

Global deep learning model for delineation of optically shallow and optically deep water in Sentinel-2 imagery

Galen Richardson[a], Neve Foreman[a], Anders Knudby[a,b,*], Yulun Wu[a], Yiwen Lin[a]

[a] Department of Geography, Environment and Geomatics, University of Ottawa, 75 Laurier Avenue East, Ottawa, Ontario K1N 6N5, Canada
[b] Liquid Geomatics Ltd., 91 Brighton Avenue, Ottawa, Ontario K1S 0T3, Canada

ARTICLE INFO

Edited by: Dr. Menghua Wang

Keywords:
Optically deep/shallow water
Deep learning
Sentinel-2
Aquatic remote sensing
Neural network

ABSTRACT

In aquatic remote sensing, algorithms commonly used to map environmental variables rely on assumptions regarding the optical environment. Specifically, some algorithms assume that the water is optically deep, i.e., that the influence of bottom reflectance on the measured signal is negligible. Other algorithms assume the opposite and are based on an estimation of the bottom-reflected part of the signal. These algorithms may suffer from reduced performance when the relevant assumptions are not met. To address this, we introduce a general-purpose tool that automates the delineation of optically deep and optically shallow waters in Sentinel-2 imagery. This allows the application of algorithms for satellite-derived bathymetry, bottom habitat identification, and water-quality mapping to be limited to the environments for which they are intended, and thus to enhance the accuracy of derived products. We sampled 440 Sentinel-2 images from a wide range of coastal locations, covering all continents and latitudes, and manually annotated 1000 points in each image as either optically deep or optically shallow by visual interpretation. This dataset was used to train six machine learning classification models - Maximum Likelihood, Random Forest, ExtraTrees, AdaBoost, XGBoost, and deep neural networks - utilizing both the original top-of-atmosphere reflectance and atmospherically corrected datasets. The models were trained on features including kernel means and standard deviations for each band, as well as geographical location. A deep neural network emerged as the best model, with an average accuracy of 82.3% across the two datasets and fast processing time. Higher accuracies can be achieved by removing pixels with intermediate probability scores from the predictions. We made this model publicly available as a Python package. This represents a substantial step toward automatic delineation of optically deep and shallow water in Sentinel-2 imagery, which allows the aquatic remote sensing community and downstream users to ensure that algorithms, such as those used in satellite-derived bathymetry or for mapping bottom habitat or water quality, are applied only to the environments for which they are intended.

1. Introduction

Mapping and monitoring of coastal and inland water ecosystems often incorporates optical satellite imagery, which can be used to derive information on water quality, water depth, and bottom habitat. Interpretation of such imagery typically relies on an assumption regarding the water's optical depth that divides the approaches used to extract environmental information from the imagery into two groups. 1) The first group of approaches assumes that the water is so deep and/or turbid that a negligible amount of the sunlight detected by the satellite sensor has been reflected off the seafloor, i.e. the water is 'optically deep water' (ODW), and thus only the optical properties of the water itself and its suspended constituents, along with sun-sensor geometry, influence the reflectance of the subsurface aquatic environment. This greatly simplifies the analysis of water quality and indicates that mapping of water depth and bottom habitat based on pixel reflectance is not possible with the optical data in question. 2) The second group of approaches assumes non-negligible seafloor reflection, i.e. that the water is 'optically shallow water' (OSW). This invalidates the simplified approaches to water quality mapping and indicates that the imagery can also be used to estimate water depth and bottom habitat.

Despite how fundamental it is to know which of these two

---

* Corresponding author at: Department of Geography, Environment and Geomatics, University of Ottawa, 75 Laurier Avenue East, Ottawa, Ontario K1N 6N5, Canada

E-mail address: aknudby@uottawa.ca (A. Knudby).

https://doi.org/10.1016/j.rse.2024.114302
Received 19 March 2024; Received in revised form 31 May 2024; Accepted 27 June 2024

assumptions is true for a given area of interest in a satellite image, there is no globally effective and automated method to assess it, and no standardized mask product akin to those available for clouds (e.g., Foga et al., 2017). As a result, most published studies of satellite-derived bathymetry either apply manual, and hence subjective, masking of optically deep water (Hamylton et al., 2015), use manually-tuned semi-automated approaches such as object-based classification (Ahola et al., 2020), or simply ignore the issue and provide estimations of bathymetry for all areas, leaving it to the user to determine which pixels contain useful information (Hedley et al., 2012; Knudby et al., 2016; J. Li et al., 2021). Nonetheless, several attempts have been made to develop and demonstrate approaches to distinguish optically deep and shallow water. The earliest that we are aware of is the 'Substratum Detectability Index' (SDI) developed by Brando et al. (2009) as part of a satellite-derived bathymetry study, in which substratum detectability is assessed on the basis of the spectral difference between the remote sensing reflectance of a pixel and the modeled remote sensing reflectance of optically deep water. For another satellite-derived bathymetry study, Caballero and Stumpf (2023) developed an approach to mask out optically deep water using two criteria, tuned to relatively clear and turbid waters respectively. The 'Near-Infrared Bottom Effect Index' (NIBEI) developed by Arabi et al. (2020) was based on a comparison between the observed reflectances in a pixel and an empirically derived threshold value for optically deep water of a ratio of remote sensing reflectances in two infrared bands. Lee et al. (2022) adopted a different approach in a study dedicated to disentangling optically deep and optically shallow waters, investigating the classification accuracy that could be obtained by applying threshold values to a range of spectral indices for a binary (optically) deep vs. shallow classification of water pixels. Lee et al. (2021) and Lai et al. (2022) instead used a neural network to perform a similar binary classification.

While these studies have demonstrated an ability to distinguish optically deep and shallow water, and to use this to inform limitations on the application of bathymetry estimates to optically shallow pixels (Brando et al., 2009; Caballero and Stumpf, 2023; Lai et al., 2022) and water quality estimates to optically deep pixels (Arabi et al., 2020), the approaches themselves have a range of limitations to broader use. Calculation of the SDI requires the use of a radiative transfer model and appropriate input data for aquatic environments, which severely limits its application. The approach developed by Caballero and Stumpf (2023) functions only as part of an empirical satellite-derived bathymetry workflow that requires the availability of (recent and high-quality) in situ data on water depth. The NIBEI is formulated only on the basis of near-infrared wavelength bands, whose limited water penetration limits its ability to provide information on whether areas are optically deep or shallow in the visible wavelengths that penetrate deeper into natural waters. More fundamentally, all of the existing approaches have only been demonstrated for a very limited set of images, often derived from a narrow range of environments. Brando et al. (2009) used a single CASI hyperspectral image, Arabi et al. (2020) used multiple Sentinel-3 images from a single location in the Wadden Sea, and while Lai et al. (2022) tested their classifier at six different sites, all of these were located in tropical coral reef-dominated environments. Caballero and Stumpf (2023) developed their approach with seven Sentinel-2 images from seven locations across the Caribbean and East coast of the United States, and Lee et al. (2022) used four Sentinel-2 images covering very different aquatic environments. These two latter studies are thus the only ones to have applied their approach across a range of environments for which water quality, seafloor reflectance, as well as sun-sensor geometry and atmospheric conditions can be expected to vary substantially. However, both studies were based on a limited set of manually selected images and did not use separate images for training and testing.

In this study, we developed a general-purpose predictive model for distinguishing optically deep and optically shallow water pixels in Sentinel-2 imagery, as identified by visual interpretation. We trained a selection of machine learning models on a large, randomly selected, and globally distributed set of images, and tested them on a separate set of images, also randomly selected and globally distributed. We made the best-performing model publicly available as a Python package, along with the data used to train and test it, as a step toward automation of the delineation of optically deep and shallow water in Sentinel-2 imagery.

2. Methods

The process used to develop the dataset and train and test the machine learning models, as well as the steps required for implementation, is outlined in Fig. 1.

2.1. Image sampling

A set of globally distributed Sentinel-2 images, representing diverse coastal environmental conditions, including variations in water depth, water quality, bottom substrate type, and atmospheric state, were sampled to form the basis for the annotation of optically deep and optically shallow water pixels. For image sampling, we used the Military Grid Reference System (MGRS), a 100 × 100 km tiling scheme based on the UTM projection system, which is the standard system used to distribute Sentinel-2 images (Bauer-Marschallinger and Falkner, 2023). Outside the polar regions, the MGRS system is based on ~8° latitude bands labeled with letters, starting with C at ~80°S and ending with X at ~84°N (omitting I and O). Polar regions, labeled with letters A and B (south), and Y and Z (north), were excluded since they contain ice-covered polar regions without coastlines and are not imaged by Sentinel-2. MGRS grid codes that did not intersect with the global coastline as defined by a 10-m vector product (Kelso, 2022) were also excluded. For MGRS grid codes with letters C, D, E and F, located around Antarctica and the Southern Ocean where a relatively small amount of coastline exists for each latitudinal band, we randomly sampled 5 grid codes per letter. For letters G, H, J and K, which have more coastline than around the Southern Ocean but less than more northern latitudes, we sampled 15 grid codes per letter, and for all other letters, which generally contain a large amount of coastline, we sampled 30 grid codes per letter. All MGRS grid codes were sampled without replacement, resulting in a total of 440 grid codes (Table 1). One Sentinel-2 image with a maximum cloud cover of 25% was then randomly sampled for each grid code. These Sentinel-2 images were visually inspected to ensure that they contained a section of visible coastline; those that did not were discarded and a new image was randomly sampled from the same MGRS grid code, resulting in a total of 440 images sampled from 440 different MGRS grid codes (Table 2, Fig. 2).

2.2. Annotation

For each image, 10 points were placed randomly along the coastline within the image extent, each marking the beginning of a transect. Transects consisting of 100 points spaced 10 m apart, heading away from land perpendicularly from the coastline, were then created, for a total of 1000 points per image. Transects that were covered by clouds, shadows cast by cloud or terrain, or located entirely on land, were moved to the nearest clear coastal location. The points in each image were then manually annotated by two researchers (GR and NF) to determine if the corresponding pixel contained optically shallow water or optically deep water. This determination was made based on whether the seafloor was visually detectable or not in the pixel, in any band. ODW can thus be caused by the water being physically deep, but it can also be a result of high turbidity, sunglint, whitecaps, breaking waves, or other environmental factors that render the seafloor undetectable in a given image, even if it is physically shallow enough that it could be detectable in another image of the same area acquired under different conditions. Visual determination of whether the seafloor is visible or not is difficult in certain cases, such as in the presence of substantial turbidity or near the depth limit of seafloor detectability; in these cases,

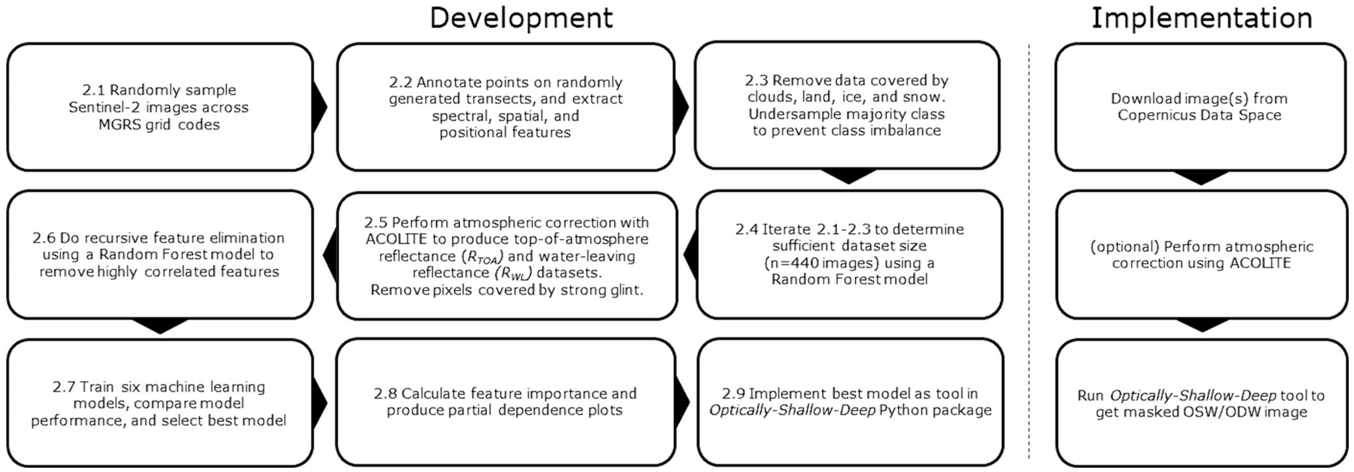

Fig. 1. Flowchart outlining the process of model development (left), and model implementation (right). Each step in the model development process is noted in the flowchart by a number that corresponds to the section (from 2.1 to 2.9) that provides further details.

Table 1
Summary of Sentinel-2 images sampled for different latitude ranges as defined by MGRS gid code letters.

MGRS grid code letters	Latitude range (°)	Images sampled per letter	Images sampled total	Notes
A-B	90 S - 80 S	0	0	Antarctica, no coastline and no Sentinel-2 images.
C-F	80 S - 48 S	5	20	Southern Ocean and southern South Atlantic; small amount of coastline.
G-K	48 S - 16 S	15	60	Southern Atlantic, Indian and Pacific Oceans; moderate amount of coastline.
L-X	16 S – 84 N	30	360	Equatorial and Northern Atlantic, Indian and Pacific Oceans; large amount of coastline.
Y-Z	84 N – 90 N	0	0	Arctic Ocean, no coastline and no Sentinel-2 images.

Table 2
Distribution of Sentinel-2 sensors and year of images in our dataset.

Year	S2A	S2B	Total
2018	7	17	24
2019	45	57	102
2020	50	50	100
2021	31	34	65
2022	39	49	88
2023	30	31	61
Total	202	238	440

manual labeling is somewhat subjective and subject to human error. We limited our individual biases and minimized human error by having each label reviewed by both researchers, in multiple rounds, reaching a consensus for the final labeling. We also evaluated the use of ICESat-2 ATL03 data for OSW/ODW identification (e.g. Lai et al., 2022), but we found this to be problematic as bathymetric photons were sometimes missing from near-coincident ATL03 data even for areas in which the seafloor was clearly visible in the Sentinel-2 imagery.

After resampling all Sentinel-2 bands to 10-m spatial resolution, we then extracted the following 168 features for each annotated point: longitude, latitude, and absolute latitude (3 features), top-of-atmosphere reflectance (R_{TOA}) values for all Sentinel-2 bands except bands 9 and 10, which are 60-m resolution bands designed for water vapor estimation and cirrus cloud detection (11 features), and kernel means and standard deviations for the same bands using kernel sizes 3, 5, 7, 9, 11, 13, and 15 centered on each pixel (means and standard deviations for 11 bands using 7 kernel sizes, 154 features) for a total of 168 features.

2.3. *Dataset cleaning and balancing*

The annotated dataset was cleaned by removing points located on land, covered by ice, snow, clouds or human-made objects such as ships and airplanes, or located in shadows from clouds or terrain. After cleaning, the ODW class comprised approximately three times as many data points as the OSW class. We therefore randomly undersampled the ODW class to prevent class imbalance during model development (Hasanin and Khoshgoftaar, 2018; Prusa et al., 2015), resulting in a dataset with 153,994 data points evenly split between the ODW and OSW classes.

2.4. *Determining sufficient dataset size*

To build the complete dataset described in sections 2.1–2.3, we used an iterative process of incrementally adding images and manually labeling 1000 points per image, regularly evaluating the ability of a model trained on the data to discriminate between ODW and OSW, until adding further images yielded negligible improvement in model performance. We initially labeled transect points for 20 images, using one randomly sampled image per MGRS grid code for model training, and added similarly generated validation and test data to ensure a 3:1:1 ratio between training, validation and test images. A Random Forest (RF) model was then calibrated on the training dataset using default settings, and its performance was evaluated against the validation data, keeping the test data set aside for evaluation of the final model (Breiman, 2001; Pedregosa et al., 2011). After this initial model performance evaluation, we added data from 20 additional training images and the corresponding number of validation and test images to maintain the 3:1:1 ratio. The RF model was then recalibrated with the new and larger training dataset, and its performance was re-evaluated with the new and larger validation dataset. This process continued until we had training data from 60 images, at which point sampling of the coastline for MGRS letters C–F was considered complete based on a visual inspection of the sampled MGRS grid codes for that latitudinal band (Fig. 2). In subsequent iterations we thus added only 16 images from MGRS letters G-X, until the training data size reached 156 images, at which point sampling of the coastline

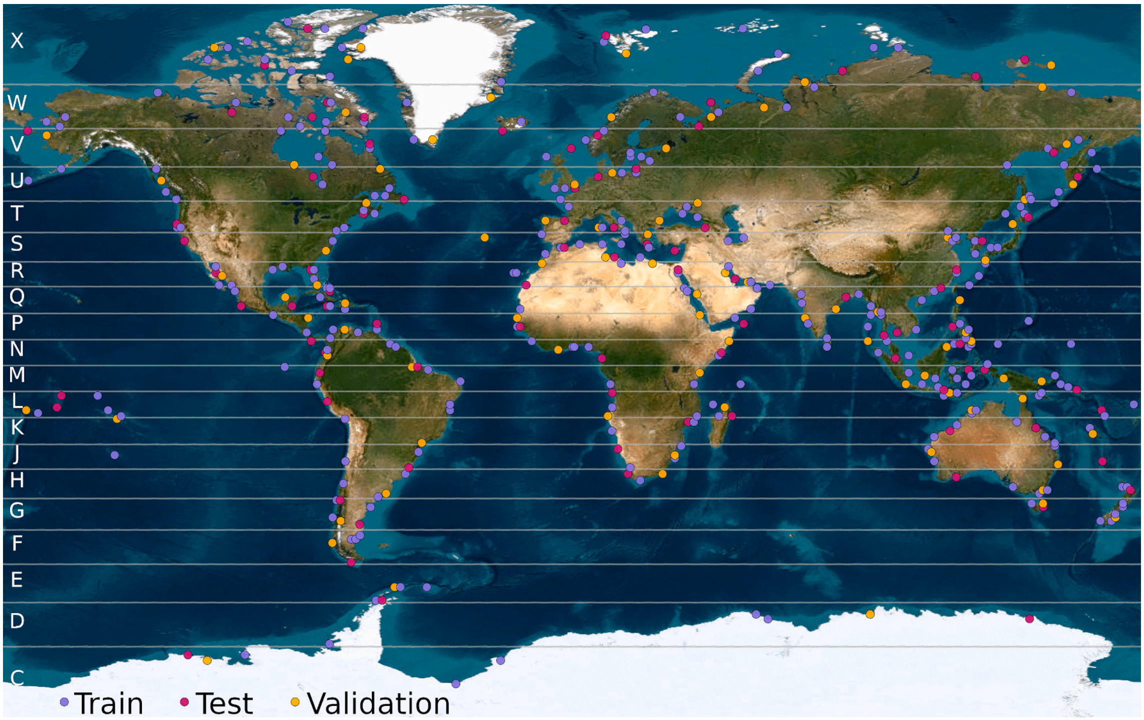

Fig. 2. The global distribution of the 440 Sentinel-2 images that constituted the final dataset. Letters used for MGRS grid codes are shown on the left.

for MGRS letters G-K was also considered complete. For the remaining iterations, we thus added only 12 images from MGRS letters L-X. The dataset creation concluded when the accuracy improvement of the RF model from each iteration was deemed negligible (Fig. 3), resulting in a total of 440 sampled images distributed across the global coastline (Fig. 2). This collection included 264 training images, 88 validation images, and 88 test images (Table 1, Table 2).

2.5. *Atmospheric correction*

To test the influence of atmospheric correction on model performance, we used the dark spectrum fitting technique in ACOLITE (version: 20231023.0), an atmospheric correction (AC) processor developed at the Royal Belgian Institute of Natural Sciences (Vanhellemont, 2019; Vanhellemont and Ruddick, 2018), to estimate water-leaving reflectance (R_{WL}) from the Sentinel-2 R_{TOA} imagery. This method automatically selects a band with the lowest values after Rayleigh-scattering correction for estimating aerosol optical thickness, and has shown good performance for coastal and inland water applications (Pahlevan et al., 2021). The two resulting datasets and models will henceforth be referred to as R_{TOA} (for the top-of-atmosphere reflectance data/models) and R_{WL} (for the water-leaving reflectance data produced by ACOLITE, and the models based on those data). Glint removal was enabled in the AC processing, extrapolating glint reflectance from the short-wave infrared to the near-infrared and visible wavelengths (Harmel et al., 2018); glint-affected pixels were removed from both the R_{TOA} and the R_{WL} datasets to allow an unbiased comparison between the two.

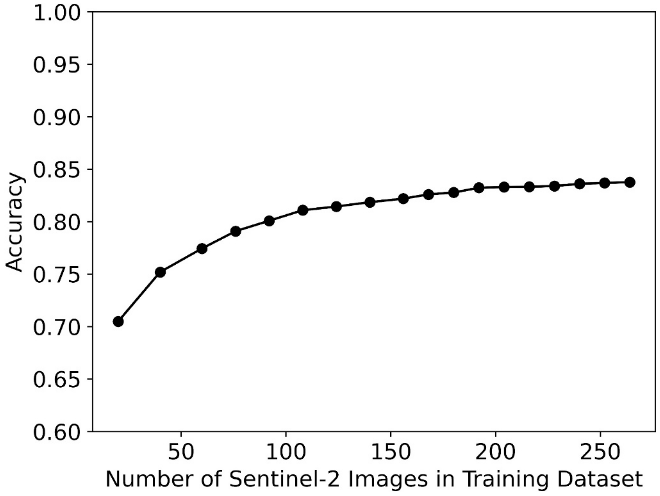

Fig. 3. Accuracy of the RF model with default settings, as a function of the number of Sentinel-2 images used to train the model. Dataset creation proceeded iteratively until further addition of images produced negligible accuracy improvement.

2.6. *Feature reduction*

In machine learning, the elimination of uninformative and redundant features is essential for lowering model complexity and increasing training speed and model performance (R.-C. Chen et al., 2020; Genuer et al., 2010; Kwon et al., 2022; Liu et al., 2021). The dataset described above consisted of 168 features, many of which were highly correlated. We therefore implemented a recursive feature elimination (RFE) strategy, based on a RF model, to derive a smaller set of features and improve predictive performance (Behnamian et al., 2017; Díaz-Uriarte and de Andrés, 2004; Genuer et al., 2010). First, the mean permutation feature importance was calculated on the validation dataset for 20 RF models trained with default settings (Altmann et al., 2010; Behnamian et al., 2017; Pedregosa et al., 2011). The 20% of features with the lowest permutation importance were then iteratively removed, the 20 models retrained, and the mean feature importance recalculated (Behnamian et al., 2017; Díaz-Uriarte and Alvarez de Andrés, 2006; Genuer et al., 2010). This iterative process was stopped at the last iteration for which the reduced set of features produced a validation accuracy <0.01 from the highest accuracy achieved by any set of 20 models, since too few features can result in poor performance (Díaz-Uriarte and de Andrés, 2004). After stopping the RFE, the lowest number of features that produced an accuracy within one standard deviation from the highest accuracy was considered the optimal feature set (Breiman et al., 2017; Díaz-Uriarte and de Andrés, 2004; Ripley, 1996). As a result of this process, 20 features were selected from the R_{TOA} dataset, as model performance decreased substantially with further elimination of features (Fig. 4A). Only 13 features were selected from the R_{WL} dataset (Fig. 4B). Both RFE processes resulted in a > 1.4 percentage point performance increase on the validation dataset compared to using all features. The retained features included absolute latitude, longitude, as well as features derived from bands 1, 2, 3, 4, 5, 8, and 11 (Fig. 4, Fig. 5). We repeated this feature elimination process for the other models used in our study (listed in section 2.7) but retained the features selected by the RF for all models to facilitate feature importance evaluation, and because this model produced higher accuracy on the validation dataset than the other models did with their respective reduced feature sets. One exception was the Dense Neural Network (DNN) model, whose structure was only developed after feature elimination was performed due to the lengthy trial and error development process required to make a high-performing DNN model (Knudby and Richardson, 2023; Abdolrasol et al., 2021).

To specifically evaluate the value of neighborhood information (Knudby and Richardson, 2023) we also created R_{TOA} and R_{WL} datasets each using only a set of features derived from single pixels, i.e. excluding all kernel-based features.

2.7. Model development

We evaluated six predictive models for both the R_{TOA} and R_{WL} datasets as well as the single-pixel R_{TOA} data: maximum likelihood classifier (MLC), RF, extremely randomized trees (ExtraTrees), AdaBoost, extreme gradient boosting (XGBoost), and neural networks. All models predicted the probability of data points belonging to the OSW class and by default applied a 50% probability threshold to generate a binary OSW/ODW classification. Each model was optimized using a grid search method to select the combination of model configuration parameters that resulted in the highest accuracy when the model was compared to the validation data (Lerman, 1980; Richardson et al., 2023a). After this optimization, the training and validation datasets were combined to train the final model for all models except the neural networks, and performance was assessed by comparison of model predictions to the annotated test dataset. The DNN models had separate training and validation datasets throughout model development since this was required for backpropagation. Identification of the best model for implementation in the Python package was based on a combination of prediction accuracy and processing time.

2.7.1. Maximum likelihood classifier

MLC (Myung, 2003; Pedregosa et al., 2011) is a predictive model that uses a log-likelihood function with the assumption that data are independently and identically distributed (Eliason, 1993; Strahler, 1980). We used the 'Logit' function from the *statsmodels* package to compute the maximum likelihood for each pixel (Seabold and Perktold, 2010). We optimized the maximum number of iterations (5, 10, 15, 20, 25, 30) and the solver from the available set of methods ('newton', 'bfgs', 'lbfgs', 'powell', 'cg', and 'ncg').

2.7.2. RF classifiers

RF is an ensemble machine learning method based on a collection of decision trees, in which a 'vote' is produced by each tree and the majority vote becomes the final model prediction (Breiman, 2001; Maxwell et al., 2018). We used the RandomForestClassifier and ExtraTreesClassifier available in the *scikit-learn* package (Pedregosa et al., 2011). The ExtraTreesClassifier is an adaptation of a Random Forest that implements extremely randomized decision trees to reduce variance (Geurts et al., 2006). For both classifiers, we optimized the numbers of trees (25, 50, 100, 250, 500, 1000), and the criterion used to evaluate the quality of each split ('gini', 'entropy', 'log_loss').

2.7.3. Boosting models

Boosting is a concept used to maximize the performance of an ensemble learning algorithm by iteratively improving its ability to make correct predictions for difficult data points (Schapire and Freund, 2012). We evaluated AdaBoost (Schapire, 2003) and XGBoost, implemented with the *scikit-learn* and *XGBoost* packages respectively (T. Chen and Guestrin, 2016; Pedregosa et al., 2011). The AdaBoost algorithm is designed to adapt to the errors of an ensemble model by iteratively updating the weights of individual learners in the ensemble, and the weights of data points, as additional algorithms are added to the ensemble (Freund and Schapire, 1997). XGBoost is based on the principle of gradient descent, where in each iteration the function chooses the most efficient path toward minimizing the loss function (Friedman, 2001; Natekin and Knoll, 2013). The model configuration parameters optimized for these included the learning rate (0.0001, 0.001, 0.01, 0.1; XGBoost only) and the number of boosting stages (25, 50, 100, 250, 500, 1000; both models).

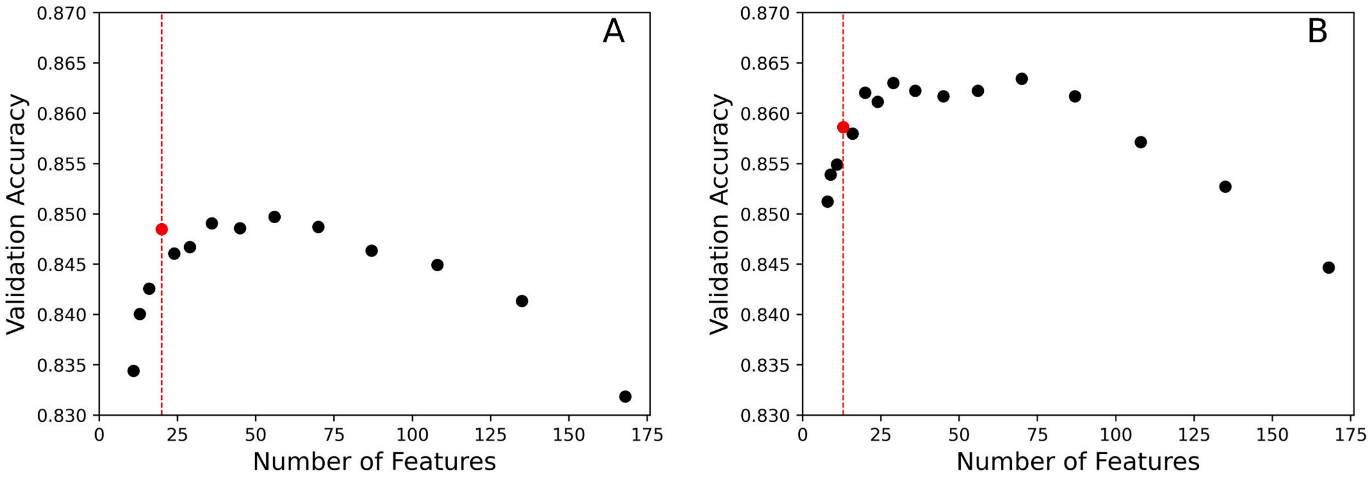

Fig. 4. Model validation performance as a function of the number of features used for model training, for the R_{TOA} (A) and R_{WL} (B) datasets. The red points represent the selected number of features for each dataset. (For interpretation of the references to colour in this figure legend, the reader is referred to the web version of this article.)

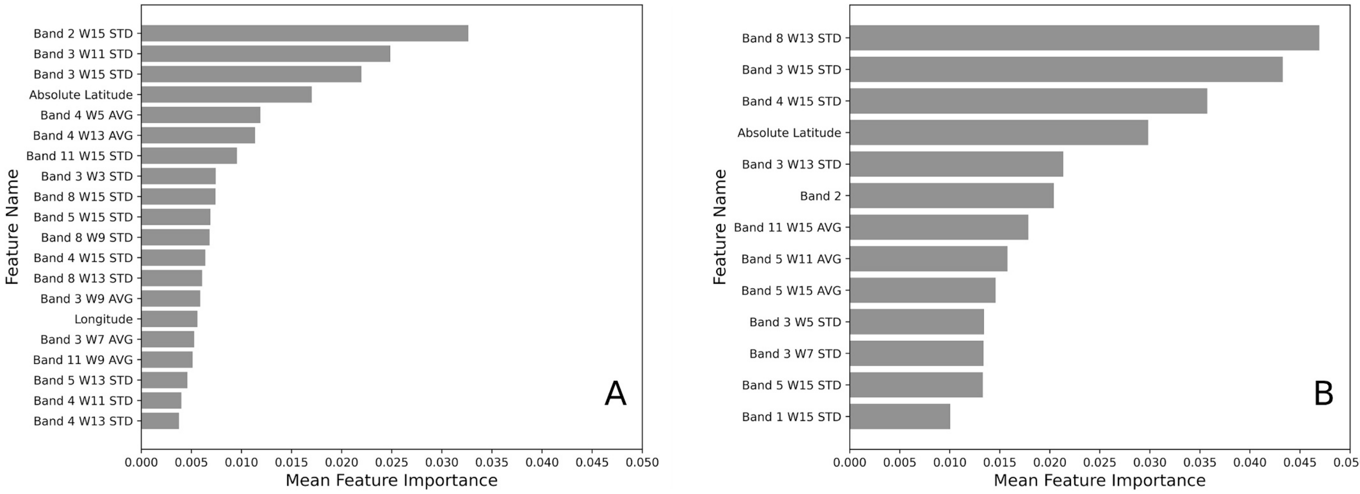

Fig. 5. Mean feature importance of the selected features for the R_{TOA} (A) and R_{WL} (B) models from RFE using an RF model. The number following the "W" in the feature names corresponds to the window (kernel) size. SD/AVG indicate the standard deviation/mean of pixel values within the kernel of the corresponding window size.

2.7.4. *Deep neural networks*

Neural networks are composed of layers of self-optimizing neurons consisting of weights; such models are considered to be deep neural networks (DNN) if they contain more than three hidden layers (Maxwell et al., 2018; Nazari and Yan, 2021). Neural networks learn by iteratively altering their weights through backpropagation to optimize model performance. The neural network models assessed in this study were fully-connected dense neural networks built in TensorFlow 2.8 with a number of hidden layers between 1 and 10 (L. Zhong et al., 2019). All layers had the same number of neurons; different numbers of neurons per layer were assessed (32, 64, 128, 256, 512, 1024), resulting in a wide range of model configuration parameters (L. Zhong et al., 2019). Different learning rates (0.001, 0.0001) and steps per epoch (25, 50, 75, 100) were assessed in the grid search. All models used the Adam optimizer, with a sigmoid activation function for the last layer, while all hidden layers used a Leaky ReLU activation function (Kingma and Ba, 2017). An early stopping function with a patience of 10 was implemented to prevent model overfitting. The neural network that performed the best on the validation dataset and did not show signs of overfitting was selected for each model (Rezaei and Sabokrou, 2023; Salman and Liu, 2019). A DNN with six hidden layers and 32 neurons per layer was optimal for the R_{TOA} dataset, while a DNN with four hidden layers and 64 neurons per layer was optimal for the R_{WL} dataset (Fig. 6). During model development, the R_{TOA} and R_{WL} neural network models took an average of 39 and 45 s respectively to train using an Nvidia RTX 3070ti graphics card.

2.8. *Model interpretation, feature importance and partial dependence*

To provide an understanding of the relative importance of the retained features in the best-performing model, and of how that model quantifies interactions between those features and the predicted probability of data points belonging to the OSW class, we calculated feature importances and produced partial dependence plots (PDPs) for that model. These post-hoc analyses can provide an understanding of why a model makes a certain prediction given different input data (Barredo Arrieta et al., 2020). However, feature importance and PDPs are necessarily simplifications and do not capture the full complexity of machine learning models (Barredo Arrieta et al., 2020; Ghorbani et al., 2019).

Feature importance was calculated iteratively for each feature as the decrease in model accuracy caused by the permutation of that feature's values in the test data set (Breiman, 2001). PDPs were then created for the five most important features to test the dependence of the output on the feature of interest. For each of those features, this was done by i) randomly sampling values for all features other than the feature of interest, and then ii) making predictions of OSW probability with the model, using these randomly sampled values along with a range of 100 values for the feature of interest, equally spaced between its actual minimum and maximum values. Calculations of both feature importance and partial dependence were repeated 100 times, reporting the mean results.

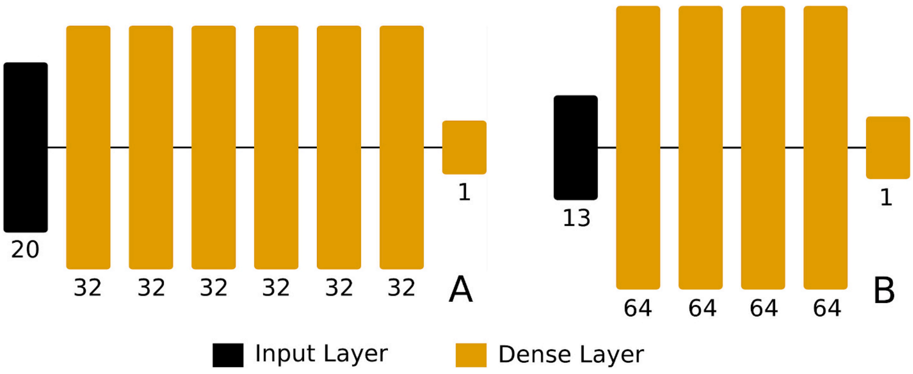

Fig. 6. The architecture for the R_{TOA} (A) and R_{WL} (B) DNN models visualized using Net2Vis (Bäuerle et al., 2021).

2.9. Creation of Python package

The two DNN models, applied to the R_{WL} and R_{TOA} data respectively, were implemented in a Python package named Optically-Shallow-Deep. This package incorporates pre-processing steps to exclude non-water and compromised-quality water pixels before applying the models. Specifically, land and snow pixels are filtered out by removing pixels with NDWI <0 (McFeeters, 1996) and NDSI >0.42 (Burns and Nolin, 2014). Strong glint is removed by excluding pixels with R_{WL} or R_{TOA} at 1600 nm > 0.05 (Vanhellemont, 2023). Additionally, cloudy pixels are masked by the built-in cloud mask of Sentinel-2 images, expanded by a buffer of 8 pixels. The code, installation instructions, and a quick-start tutorial can be accessed at https://github.com/yulunwu8/Optically-Shallow-Deep.

3. Results

3.1. Model and dataset performance comparison

The performance of all models on both datasets is shown in Table 3. All models except ExtraTrees performed better on the R_{WL} dataset than on the R_{TOA} dataset. Differences between the top-performing models were negligible for both datasets. The DNN had an accuracy of 0.820 on the R_{TOA} dataset, while the RF and XGBoost models had accuracies of 0.818 and 0.817 respectively. On the R_{WL} dataset, the RF and XGBoost models had accuracies of 0.826, while the DNN had an accuracy of 0.825. The RF, XGBoost, and DNN models exhibited the highest average accuracies across the two datasets.

Model precision and recall (Fawcett, 2006), two additional performance metrics, were also calculated for the three best models (RF, XGBoost, DNN; Table 4), to assess bias in their predictions. For a given class, precision quantifies the proportion of positive identifications that were correct, while recall quantifies the proportion of true positives identified correctly. Using the OSW class as an example, precision is calculated as the proportion of all pixels identified as OSW that were actually OSW, i.e. the true positives divided by all positives. Similarly, recall is calculated as the proportion of OSW pixels that were identified as OSW, i.e. true positives divided by the sum of true positives and false negatives. All models had greater precision than recall for the OSW class and greater recall than precision for the ODW class, indicating an underestimation of the OSW class in the model predictions. This tendency was strongest for the RF model and was negligible only for the DNN model applied to the R_{WL} dataset.

3.2. Model prediction time comparison

We evaluated the time required for the three best models to make predictions by randomly sampling 30,000,000 water pixels, approximately 25% of a Sentinel-2 scene, from the test dataset. The RF and XGBoost models used the predict function in *scikit-learn* and *XGBoost* respectively, while the DNN used the *tensorflow* predict_on_batch function to process the sampled dataset. All models were assessed on an Intel i5-12600k processor using all 10 cores with 64 GB of DDR4 RAM. The DNNs outperformed the other models, taking <6 s to process 30,000,000 pixels in both datasets (Table 5). Given their high accuracy, low bias, and computational efficiency, the DNN models were selected for use in the Python tool to delineate OSW and ODW in Sentinel-2 images.

The time required to read a Sentinel-2 image and create a map of ODW and OSW is substantially longer than making predictions with the DNN models, primarily due to the creation of the features using kernel statistics. We therefore also compared the time it took to completely process a set of ten Sentinel-2 images, which averaged 28 min per R_{TOA} image and 32 min per R_{WL} image, the latter including the 9 min it took on average to perform the atmospheric correction in ACOLITE.

Table 3
Comparison of machine learning model performance for the R_{TOA} and R_{WL} datasets.

Model	R_{TOA}	R_{WL}	Mean model accuracy
MLC	0.752	0.777	0.765
RF	0.818	0.826	0.822
ExtraTrees	0.812	0.790	0.801
AdaBoost	0.790	0.810	0.800
XGBoost	0.817	0.826	0.822
DNN	0.820	0.825	0.823
Mean dataset accuracy	0.802	0.809	0.806

Table 4
Accuracy, precision and recall metrics for the three best models.

Dataset	Model	Precision / Recall, OSW	Precision / Recall, ODW
R_{TOA}	RF	0.887 / 0.729	0.770 / 0.907
	XGBoost	0.860 / 0.757	0.783 / 0.877
	DNN	0.859 / 0.766	0.789 / 0.874
R_{WL}	RF	0.876 / 0.760	0.788 / 0.893
	XGBoost	0.860 / 0.779	0.798 / 0.874
	DNN	0.825 / 0.824	0.824 / 0.825

3.3. Map output

To illustrate model performance on Sentinel-2 imagery, we applied the DNN models to a diverse set of images from the test dataset (Fig. 7). Fig. 7A and B, which show coral reefs near Jamaica and turbid water in the Baltic Sea, respectively, were based on the R_{WL} model. The prediction of OSW/ODW in Fig. 7A aligned well with visual interpretation except for the region with/near whitecaps in the red box, while there was a noticeable overestimation of OSW in the high-turbidity environment shown in Fig. 7B. Fig. 7C and D, which show a wavy nearshore environment in Australia and a turbid lower Arctic coastline, respectively, were based on the R_{TOA} model. Predictions in both Fig. 7C and D aligned well with visual interpretation, with a slight overestimate of the extent of OSW in Fig. 7C. While much of the seafloor is obscured due to the high-turbidity conditions in Fig. 7D, the model tended to correctly predict OSW near the coastline.

3.4. Feature importance and PDPs

To further our understanding of how the selected models made predictions, feature importances and PDPs were created for the R_{TOA} (A) and R_{WL} (B) DNN models following the methodology outlined in section 2.8 (Fig. 8 and Fig. 9 respectively). The two most important features across both models were standard deviation calculations using band 3 and a large kernel size. Additional features with high importance included mean values within large kernels, based on band 3 (R_{TOA}) and band 5 (R_{WL}). The locational features, longitude and absolute latitude, had low feature importances, and several features in both models had negative feature importances. While the latter indicates that the performance of the DNN model could possibly have been improved if these features had been eliminated, the issue is complex because eliminating features from a DNN requires not just re-training the model but also a re-evaluation of the model structure (Fig. 6).

The PDPs for the R_{TOA} and R_{WL} models both indicate that higher feature values for the three most important features lead the models to predict higher OSW probability (Fig. 9). Pixels with higher standard deviation in band 3, calculated for a large kernel (size 11–15), lead both models to predict higher OSW probability. For the R_{TOA} model, the Band

Table 5
Prediction time comparison for the three best models.

	DNN	XGBoost	RF
R_{TOA}	5.57 s.	20.24 s.	390.76 s.
R_{WL}	5.65 s.	38.36 s.	377.03 s.

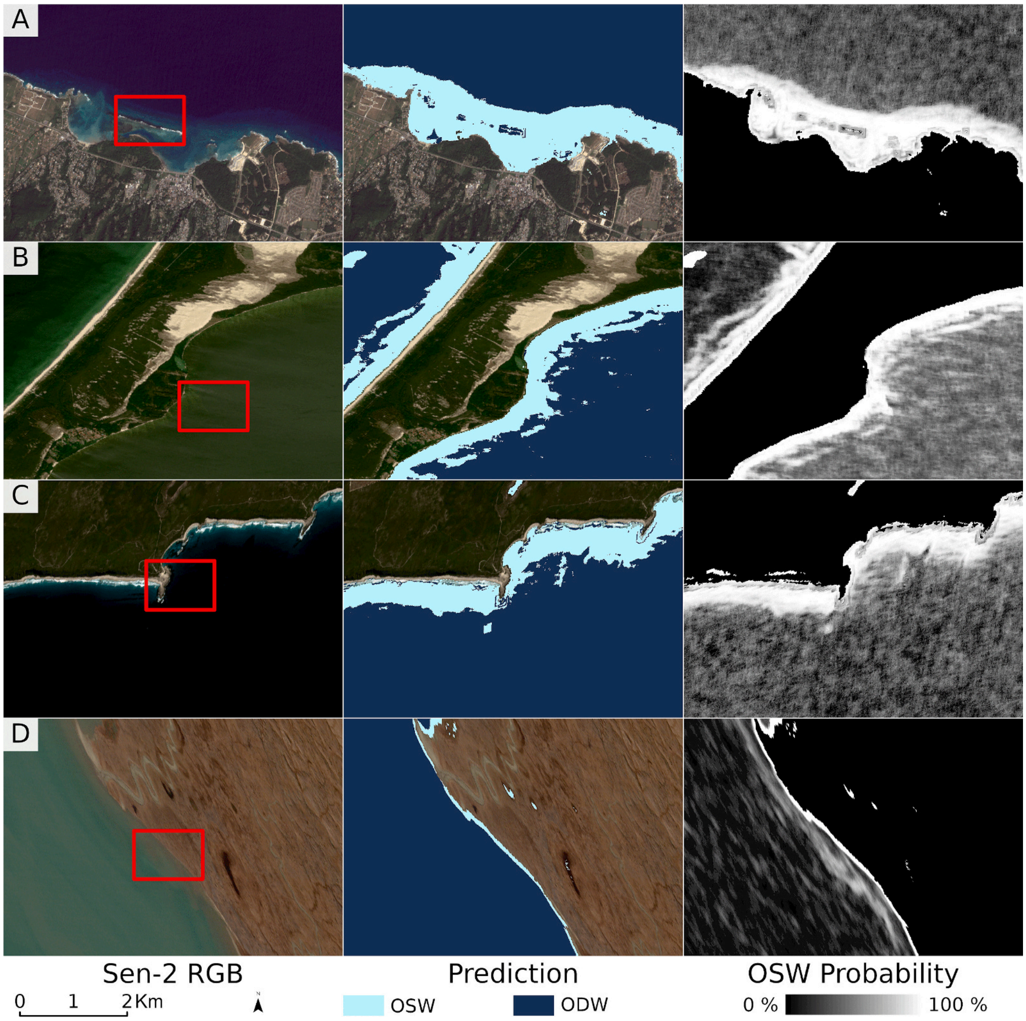

Fig. 7. Four Sentinel-2 images and their model predictions. RGB composite (left), OSW/ODW class predictions (center), and OSW probability predictions (right) from the R_{WL} (A, B) and R_{TOA} (C, D) DNN models. The red boxes correspond to zoomed in images found in Fig. 13. Additional example scenes can be found in the Appendix. (For interpretation of the references to colour in this figure legend, the reader is referred to the web version of this article.)

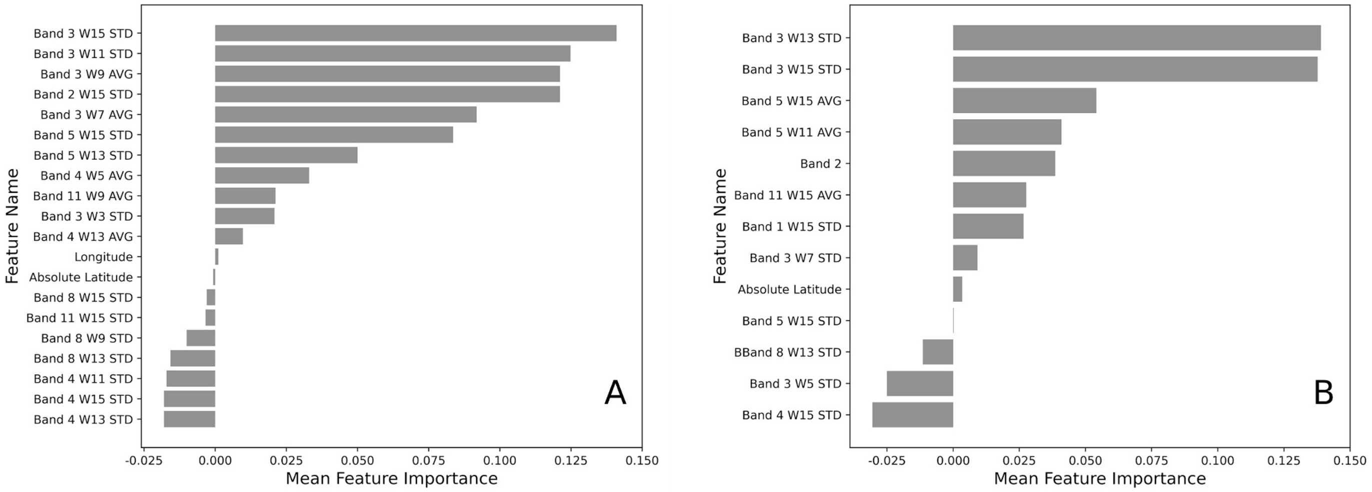

Fig. 8. Mean feature importance of the selected features for the R_{TOA} (A) and R_{WL} (B) DNN models.

3 W7 AVG feature has a downward trend (OSW probability decreases with increasing feature value), while the opposite is true for the Band 3 W9 AVG feature. Given the extremely high correlation between these variables ($R > 0.99$), the trends of these two features do not illustrate direct relationships between the individual features and the response (OSW probability), but rather how they combine and partially balance

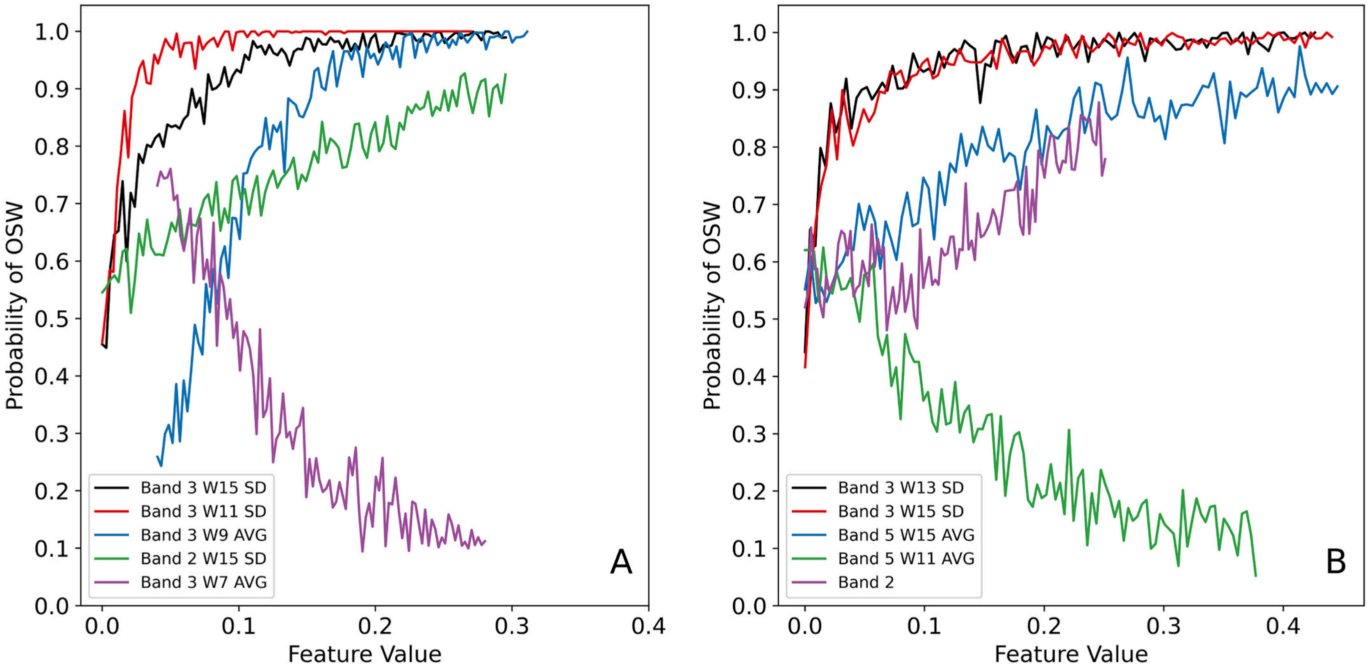

Fig. 9. PDPs for the R_{TOA} (A) and R_{WL} (B) DNN models, showing the top five most important features.

each other out in the model.

A similar pattern is seen for the R_{WL} model, involving the Band 5 W11 AVG and Band 5 W15 AVG features.

The comparison of the performance of models trained on the single-pixel vs. the full R_{TOA} dataset (Table 6) further illustrates the importance of the kernel-based features. All the models using the full R_{TOA} dataset outperform all the single-pixel models. Similar results were obtained for the R_{WL} models.

4. Discussion

4.1. Data and model considerations

The randomization of image selection used in this study is essential for building a global dataset that is genuinely representative of conditions found across all Sentinel-2 imagery that corresponds to the selection criteria - in this case a maximum of 25% cloud cover. However, such random image selection is not common practice among studies delineating ODW and OSW, leading model performance assessments in the literature to be generally optimistic and valid only for manually selected images that are typically of high quality. This is not the case for the model performance assessment reported for our models.

For all model types except one, the R_{WL} model outperformed the R_{TOA} model; in other words, the application of atmospheric correction produced a small but consistent improvement in the models' ability to discriminate optically deep and optically shallow water. However, the small difference in accuracy, less than one percentage point on average (Table 3), suggests that atmospheric correction is not crucial for this task, especially given the additional time it requires and the challenge it can pose, e.g. for composite imagery that lacks the requisite metadata for atmospheric correction.

Table 6
Comparison of model performance for the single-pixel models and the models that include kernel-based features, for the R_{TOA} dataset.

Model	Single-pixel R_{TOA} data	R_{TOA} data
MLC	0.717	0.752
RF	0.709	0.818
ExtraTrees	0.715	0.812
AdaBoost	0.719	0.790
XGBoost	0.720	0.817
DNN	0.739	0.820
Mean dataset accuracy:	0.720	0.802

Two decisions made during the data creation process may have affected the model comparison results in favor of the RF model: i) The iterative addition of images that was used to determine a sufficient dataset size was terminated when additional data led to negligible improvement in the performance of a RF model, and ii) the recursive feature elimination yielded a set of features that were optimal for a RF model. It is possible that other model types would have been able to use additional data, or additional or different features, to improve their performance, and that their potential performance therefore is underestimated in Table 3 because they were trained with a dataset optimized for a RF model. Such decisions regarding dataset creation must sometimes be made without full knowledge of their consequences because investigating the effect of all possible combinations of options for dataset creation is practically unfeasible.

4.2. Kernel-based features

The models were trained on features derived from the individual pixels in which the labeled data points were found, as well as features describing mean and standard deviations of values within kernels centered on those pixels. The maximum kernel size used in this study was 15; larger kernels were tested (up to size 99) but not used because they produced models with similar or inferior performance while increasing the computational requirements. To our knowledge, with one recent exception (Sharr et al., 2024), all previous studies that aimed to delineate OSW and ODW have developed models based only on features derived from the individual pixels. The comparison of performances between single-pixel and kernel-based models clearly demonstrates the increase in accuracy provided by the kernel-based features, across all model types and regardless of atmospheric correction (Table 6). This is consistent with other aquatic remote sensing studies that have demonstrated that the inclusion of neighborhood information can improve model performance (Aptoula and Ariman, 2022; Knudby and Richardson, 2023; H. Li et al., 2024; J. Zhong et al., 2022). This result is also intuitively sensible; because of the apparent spectral similarity between deep water and dark seafloors in some shallower waters, determination of seafloor detectability is substantially based on spatial context in addition to the reflectance spectrum of individual pixels. A simple illustration (Fig. 10) demonstrates this: it is relatively easy to determine from visual inspection that the area shown in Fig. 10A is optically shallow, because the continuity of the spatially heterogeneous seafloor habitat is obvious in the image (note that while the models do not "see" the spatial configuration of pixels shown in Fig. 10A, they have access to information about the means and standard deviations of values within a range of kernel sizes). However, it is not at all obvious from visual inspection only of Fig. 10B whether the single pixel shown, which is the center pixel from Fig. 10A, is optically shallow or deep.

Nonetheless, the use of kernel-based features, specifically those that are highly correlated and have opposite individual influence on model predictions, is also the cause of some of the visually obvious misclassifications produced by the DNN models. An example is shown in Fig. 11A, which illustrates a site with breaking waves also shown in Fig. 7A (left panel), the binary R_{WL} model predictions (center panel), and the difference in the values of two highly correlated kernel-based features: Band 5 W11 AVG and Band 5 W15 AVG ($R = 0.98$, right panel). While it is important to keep in mind that these are not the only, or even the most important, features used by the model to make predictions, the similar spatial patterns between the center and right panels show that large positive differences in the values of these two features, seen in the area at/near the breaking waves (white area, right panel), tend to produce incorrect ODW model predictions for the area near the breaking waves (dark blue area, center panel). Another example of erroneous model predictions for pixels that have substantially different values in otherwise highly correlated features is shown for the R_{TOA} model in Fig. 11B. Here, a group of pixels with large differences between values in the Band 3 W15 SD and Band 3 W11 SD features ($R = 0.93$, right panel) produce a "halo" of incorrect ODW predictions (center panel) around the breaking waves near the bottom left corner of that site (left panel). Because of the high correlations between these pairs of variables, large differences between their values are rare in the training and validation dataset used in model development. It is therefore not surprising that the models perform poorly when such instances are encountered in the test dataset.

4.3. Class probabilities

Practical use of ODW/OSW delineation may take the form of masking, e.g. to exclude ODW pixels from bathymetry and bottom habitat maps, or to exclude OSW pixels from water quality maps made with algorithms that assume negligible bottom reflectance. Such masking is based on the binary model predictions, which are produced through application of a threshold to the probabilistic output, internal to each model, that describes the modeled probability of a pixel being OSW. In other words, probability values close to 0.5 indicate that the model is uncertain in its prediction, while values close to 0.0/1.0 convey model confidence that the pixel is ODW/OSW respectively. This probabilistic output has additional value in itself, partly because it provides an indication of the confidence the user should have in the resulting binary predictions, and partly because it allows a user to customize the threshold(s) applied for any given application. For example, for application to satellite-derived bathymetry where the user may require greater confidence that predictions are not made for ODW for which they would be invalid, the user could mask out pixels with probability values <0.6, or 0.7, depending on specific project requirements.

Another use of the probabilistic output is to apply two thresholds instead of one, e.g. at 0.3 and 0.7, labeling the pixels with intermediate probability values as 'unclassified'. These pixels with intermediate probability are the ones most often misclassified in the binary output, so one value of an approach with two thresholds is that it retains the pixels that are most likely to have been correctly classified as ODW or OSW. Using the results from the R_{WL} DNN model, in Fig. 12 we plotted model accuracy against progressively wider probability ranges for the 'unclassified' class, along with the number of pixels falling in the ODW/OSW classes. Including pixels with probability values between 0.4 and 0.6 in the 'unclassified' class resulted in a model accuracy of 0.853, while still classifying the large majority of the pixels. These thresholds can be selected by a user to fine-tune model outputs depending on the desired model accuracy and the tolerance for unclassified pixels in the map outputs.

To visualize the effect of using an 'unclassified' class for the map output, Fig. 13 shows zoomed-in portions of the images from Fig. 7, including a three-class output where prediction probabilities between 0.4 and 0.6 were set to "unclassified". This relatively narrow range of probability values caused a substantial reduction of misclassified pixels in Fig. 13B, and many misclassifications near the edge of where the shallow water ends were masked as unclassified in Fig. 13A and C. While not all misclassified pixels fell within the 0.4–0.6 range of probability values, it is clear from Fig. 13 that many pixels for which the correct classification was indeed uncertain were labeled as 'unclassified'.

4.4. Model prediction similarity

While model accuracies are generally similar between most models and both data sets (Table 3), a McNemar test (Lachenbruch, 2014; Pembury Smith and Ruxton, 2020) used to assess differences between DNN model predictions using the R_{TOA} and R_{WL} test datasets was highly significant ($p < 0.001$). Despite similar model accuracies (0.820 and 0.825), this shows that there is a real difference between the predictions from the two models. However, this difference disappeared ($p = 1.0$) when we removed all probability values between 0.4 and 0.6, a result that was repeated when we removed wider ranges of probability values

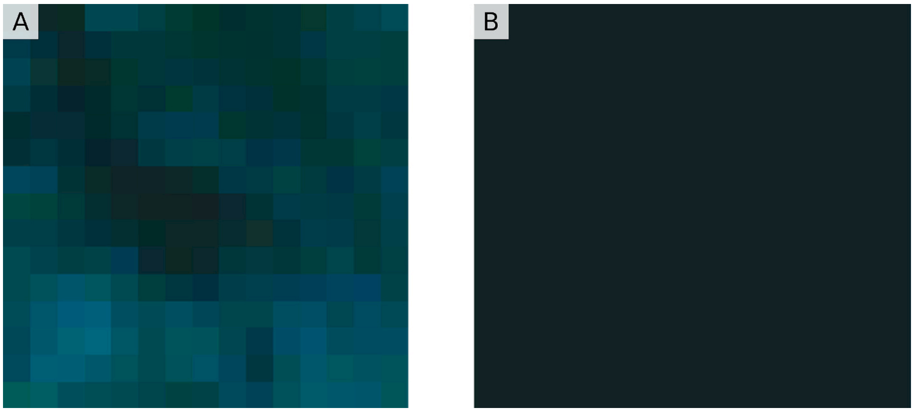

Fig. 10. A: A 15 × 15-pixel neighborhood from an optically shallow part of a Sentinel-2 image. B: The center pixel from A.

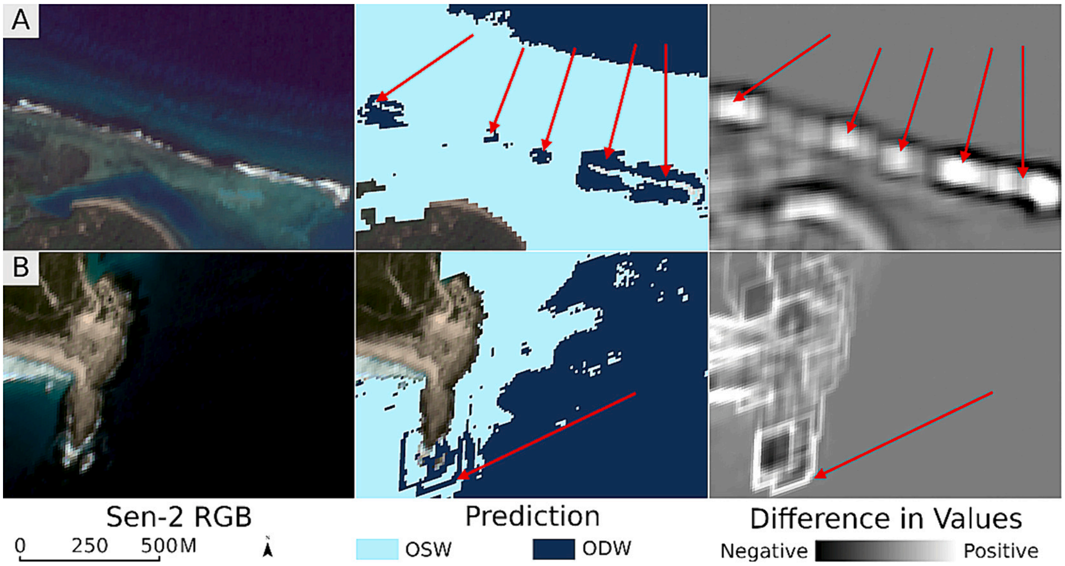

Fig. 11. Illustrations of the effect of rare feature value combinations on model predictions. A: Large positive differences between two highly correlated kernel-based features with opposite trends in the PDP (Band 5 W11 AVG and Band 5 W15 AVG) are spatially correlated with incorrect ODW predictions for optically shallow areas near breaking waves (red arrows). B: Large positive differences between Band 3 W15 SD and Band 3 W11 SD produce a "halo" effect where nearby breaking waves are within the larger kernel but not the smaller; this "halo" is also visible as incorrect ODW predictions made by the R_{TOA} model (red arrow). (For interpretation of the references to colour in this figure legend, the reader is referred to the web version of this article.)

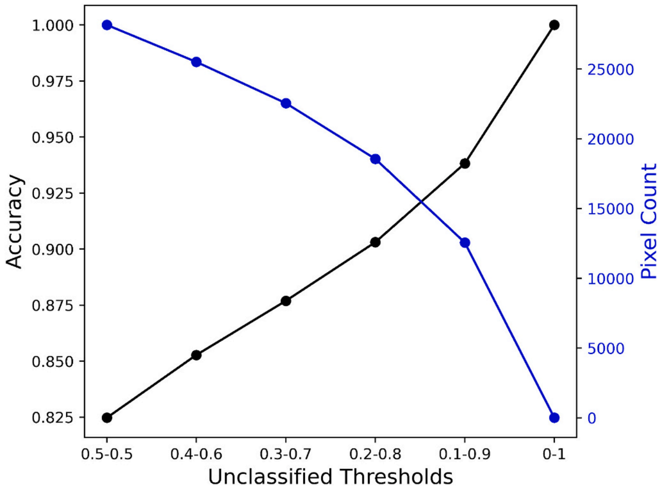

Fig. 12. The relationship between thresholds used to define the 'unclassified' class, model prediction accuracy, and pixel count for the DNN model applied to the R_{WL} dataset. The left-hand side of the fig. (0.5–0.5) corresponds to the binary model. Moving toward the right side of the figure, as the range of probabilities included in the 'unclassified' class increases, the accuracy of model predictions for the remaining pixels also, while the number of such pixels decreases, until at the right-hand side (0–1) only a negligible number of pixels with probabilities of 0 or 1 are included.

(0.3–0.7, and 0.2–0.8). This demonstrates that the DNN models for R_{TOA} and R_{WL} data differ principally in their predictions for pixels that have probabilities between 0.4 and 0.6, while the models agree for the pixels that both models are more certain about.

4.5. *Potential future improvements*

While the DNN models have performances that suggest they should be useful for some applications, their accuracy is far from perfect and some misclassifications are apparent to the human eye, such as the breaking waves (incorrectly classified as OSW) and adjacent areas (incorrectly classified as ODW) in Fig. 11. It is therefore worth exploring options to improve their performance.

4.5.1. *More or better data*

While it is often possible to improve the performance of machine learning models by adding additional high-quality training data, the regular model performance assessment performed during our iterative dataset creation process suggested that simply adding more data is not likely to be effective. The inclusion of new features, such as view and solar angles, may also have the potential to improve model performance.

Another potential improvement could come from the use of information from recent imagery of the same area to assist in the classification process, an approach that has been demonstrated for cloud detection (Champion, 2012; Tang et al., 2013). For cloud detection, the principle behind such an approach is that a sudden increase in reflectance and/or decrease in temperature is likely to indicate the presence of a cloud that was not present in previous images. A similar principle might be used to detect temporary sediment plumes that obscure the seafloor, as such plumes tend to produce an increase in reflectance and a decrease in local heterogeneity in the visible bands. We did not explore such an approach because of its requirement to include multiple recent images in the analysis of any given image, a substantial increase in model and data processing complexity over a single-image approach.

4.5.2. *Better models*

Additional model development could also be explored, such as an ensemble model based on a weighted combination of several of the top-performing models and/or other suitable machine learning model types using stacked generalization, in which predictions are made using a weighted combination of individual model outputs (van der Laan et al., 2007; Wolpert, 1992). A naïve test of ensemble modeling, using simple averaging of the six models, did show marginal improvements in accuracy; such ensemble models using R_{TOA} and R_{WL} data had accuracies of 0.822 and 0.834 respectively, compared to 0.820 and 0.826 for the highest-accuracy individual models. However, the additional computation required for ensemble modeling is substantial, and the marginal improvements in accuracy did not warrant this approach to be implemented in the Python package. Entirely different model types could also be explored. In addition to the models outlined in Section 2.7, we did

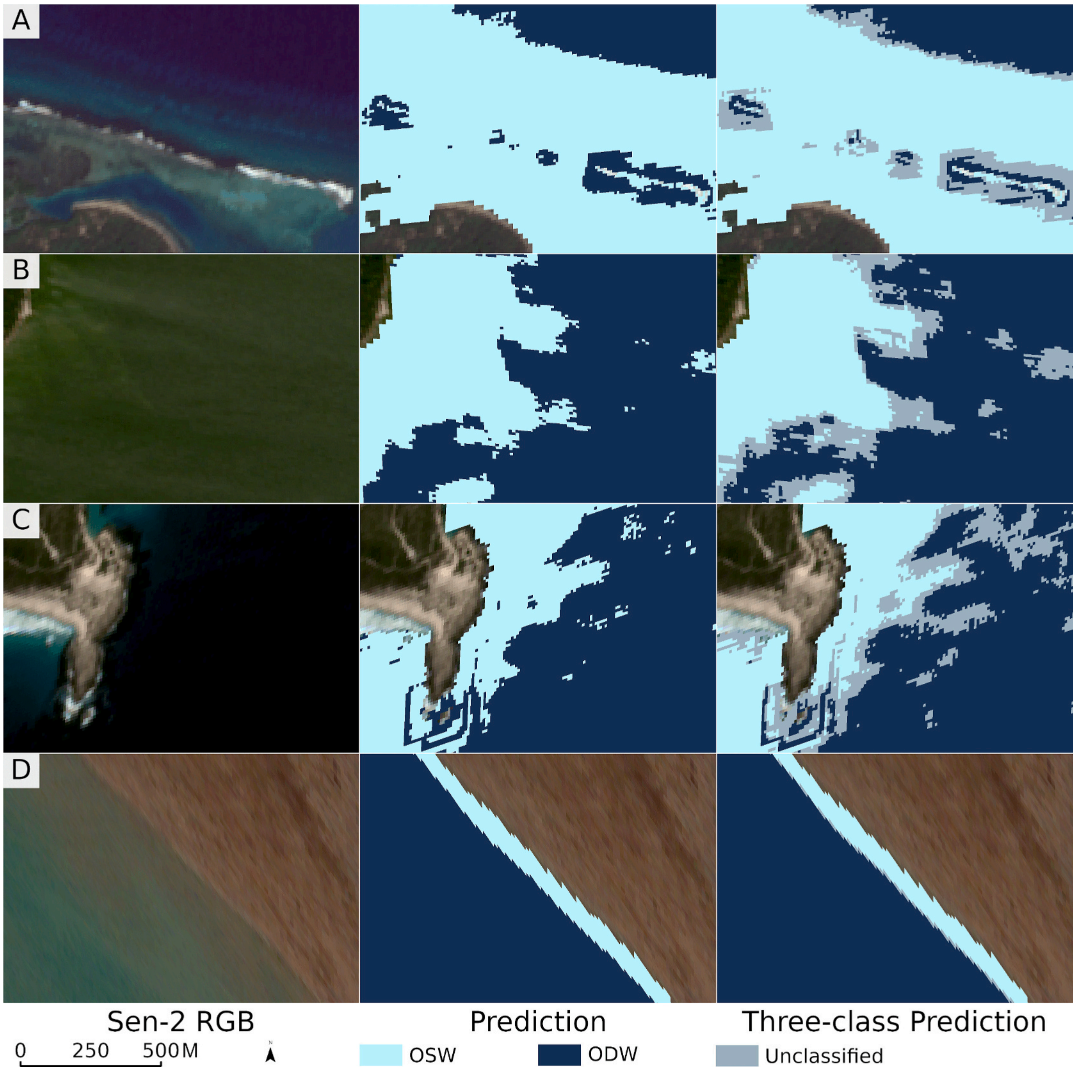

Fig. 13. Sentinel-2 images, binary predictions, and three-class predictions using an unclassified class for pixels with probability values between 0.4 and 0.6, based on the DNN model applied to the R_{WL} (A, B) and R_{TOA} (C, D) datasets. Additional examples can be found in the Appendix.

explore the possibility of implementing a convolutional neural network (CNN) inspired by published architectures that also use kernels to predict central pixel values (Al Najar et al., 2022; Knudby and Richardson, 2023; H. Li et al., 2024; Richardson et al., 2023b). However, due to the higher amount of computing power required for model training and prediction, low accuracies in early testing, and a near-infinite number of potential CNN architectures, we decided to focus on relatively simpler machine learning models more appropriate for wide adoption for the task of delineating OSW/ODW in Sentinel-2 images (Nazari and Yan, 2021). Another approach is to replace the global model with a set of regional models specifically trained for different environmental types, e.g. coral reefs, rocky temperature coasts, Arctic waters etc. A regionalized approach would allow fine-tuning of the individual models, including through optimization of kernel sizes, feature reduction, and model configuration parameters. The DNN model specifically could be retrained for regional models through transfer learning, which reduces model training time and often leads to higher performance than training an entirely new model (Ma et al., 2024; Richardson et al., 2023a; Shi et al., 2024). However, the disadvantage of a regionalized approach is the subsequent requirement for users to identify the correct model to use for a given area, or the requirement to use multiple models to cover areas that include more than one environmental type. The current global model already incorporates information on environmental type through its use of geographical location, longitude, latitude, and absolute latitude, as features.

4.5.3. *More detailed class definitions*

Improvement may also be achieved by more detailed annotation. For example, water can be optically deep due to the presence of white caps or breaking waves, high turbidity, or great physical depth. These different types of ODW have very different typical feature values. Breaking waves have high reflectance values, including in the NIR bands, and tend to have high standard deviations within kernels. Turbid water also has high reflectance across the visible bands, less so in the NIR bands, and tends to have low standard deviation within kernels. Clear but physically deep water, on the other hand, has both low reflectance and low standard derivation values. Classifying these different types of ODW pixels separately may improve model performance.

4.5.4. *Better imagery*

Finally, improvement of the quality of the Sentinel-2 imagery could lead to marginal increases in model accuracy. Banding, caused by differences in acquisition timing and relative azimuth angles between the detectors on the sensor’s two focal plane assemblies (ESA, 2024), is obvious in much Sentinel-2 imagery acquired over water, where it causes an increase in the standard deviation of pixel reflectance within kernels that overlap the band edges. Given that a high standard deviation of pixel reflectance is typically associated with optically shallow water, this leads the models to predict an increased probability of OSW near the band edges (e.g. Fig. A1, row A). Atmospheric correction algorithms can typically reduce but not eliminate this effect.

The models developed for the present study only work for Sentinel-2 imagery, but a similar approach could easily be implemented for other high- or moderate-resolution optical sensors, such as the Landsat series of sensors, for which a sufficient amount of training data can be created through visual interpretation. Application to Landsat imagery would facilitate the growing use of this dataset for aquatic applications (Ho et al., 2019; Ilori et al., 2019; Knudby et al., 2014, 2016; Pahlevan et al., 2014, 2019).

5. Conclusion

We developed a deep learning model that distinguishes optically deep and optically shallow water in Sentinel-2 imagery. Six candidate machine learning models were trained and tested on a large and globally distributed set of data created by visual image interpretation of randomly sampled Sentinel-2 imagery with a maximum cloud cover of 25%. The best model, a deep neural network applied to data atmospherically corrected with ACOLITE, achieved an accuracy of 82.5%, and can be implemented in 32 min, including atmospheric correction, for a typical Sentinel-2 scene. This accuracy was achieved on randomly sampled unseen data; higher accuracy can be expected if users manually select high-quality images to avoid challenging conditions such as breaking waves and highly turbid sediment plumes. The availability of a fully automated model that distinguishes optically deep and optically shallow water in Sentinel-2 imagery, and can be applied in ~30 min, benefits the aquatic remote sensing community and downstream users for mapping aquatic environments from optical satellite imagery. The model output can be used to ensure that other algorithms, such as those used in satellite-derived bathymetry, or for mapping bottom habitat or water quality, are applied only to the environments for which they are intended. The model is provided to the public in the form of a Python package. In addition, the code and data used to train the model is also provided, for users who want to expand the dataset or experiment further with model development.

Funding

Funding for this project was provided by the Canadian Space Agency (FAST grant 18FAOTTC04), and by the University of Ottawa (Big Idea grant GR005579).

CRediT authorship contribution statement

Galen Richardson: Writing – original draft, Visualization, Validation, Software, Methodology, Formal analysis, Data curation, Conceptualization. **Neve Foreman:** Writing – review & editing, Validation, Software, Methodology, Data curation. **Anders Knudby:** Writing – original draft, Supervision, Methodology, Funding acquisition, Conceptualization. **Yulun Wu:** Writing – review & editing, Software, Conceptualization. **Yiwen Lin:** Writing – review & editing, Conceptualization.

Declaration of competing interest

The authors declare the following financial interests/personal relationships which may be considered as potential competing interests:

Anders Knudby reports financial support was provided by Canadian Space Agency. Yulun Wu reports financial support was provided by University of Ottawa. If there are other authors, they declare that they have no known competing financial interests or personal relationships that could have appeared to influence the work reported in this paper.

Data availability

The research data and tool can be accessed on GitHub at https://github.com/yulunwu8/Optically-Shallow-Deep. We have not shared the code, but it has been described in sufficient detail in the paper to be replicable.

Acknowledgements

All Sentinel-2 satellite imagery used in this study was made publicly available by ESA's Copernicus program. The authors sincerely appreciate the input and ideas provided by Dr. Michael Sawada at the University of Ottawa, and by all members of the University of Ottawa's Shallow Water Earth Observation Laboratory.

Appendix A

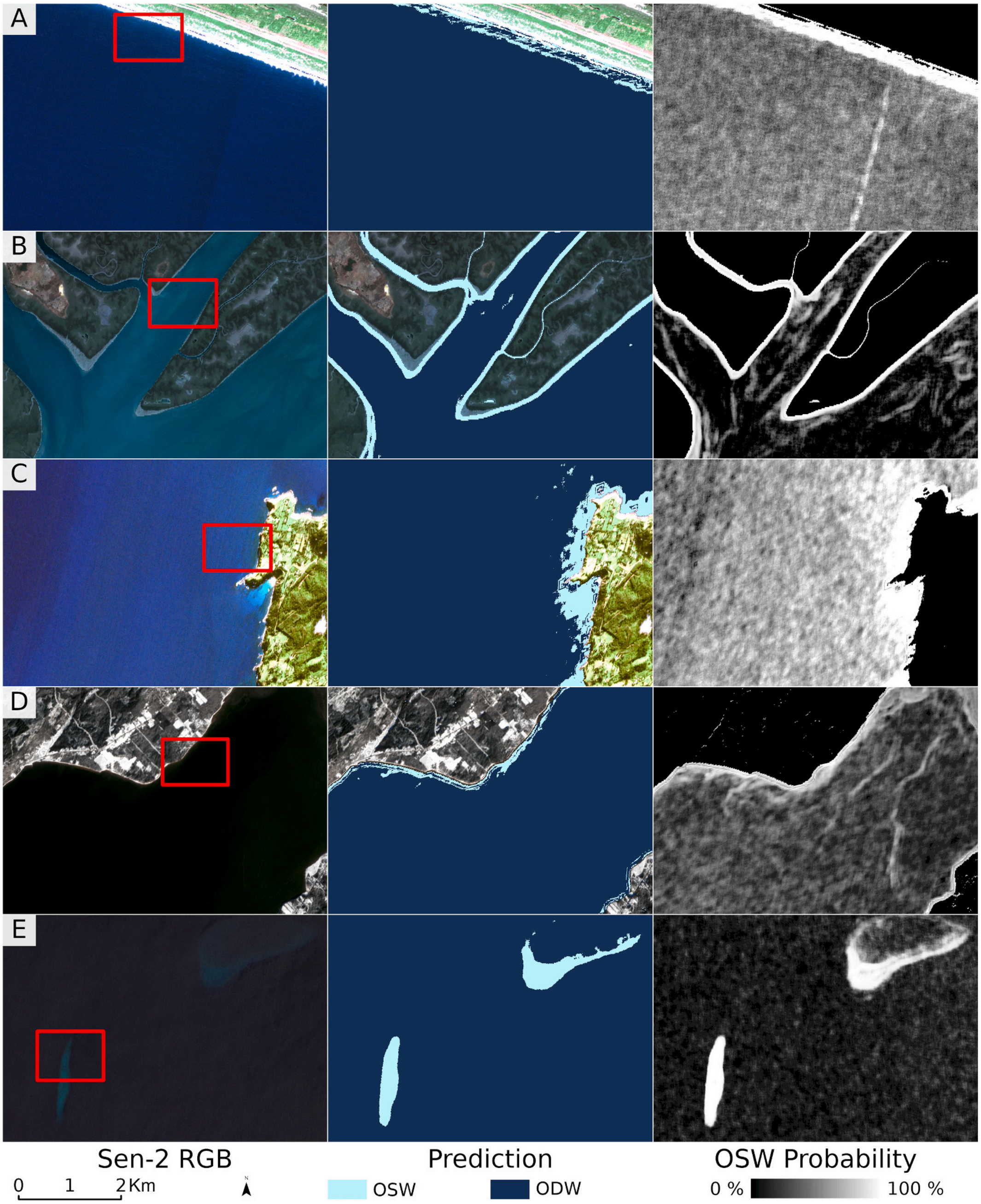

Fig. A.1. Additional scenes from the R_{WL} (A, B) and R_{TOA} (C, D, E) DNN models. The scenes are from Western Mexico, a river delta in Guinea-Bissau, coastal Norfolk Island in the Pacific Ocean, Eastern Canada, a submerged offshore reef in the Philippines for rows A, B, C, D, and E respectively. The red boxes correspond to closeups found in Fig. A.2. (For interpretation of the references to colour in this figure legend, the reader is referred to the web version of this article.)

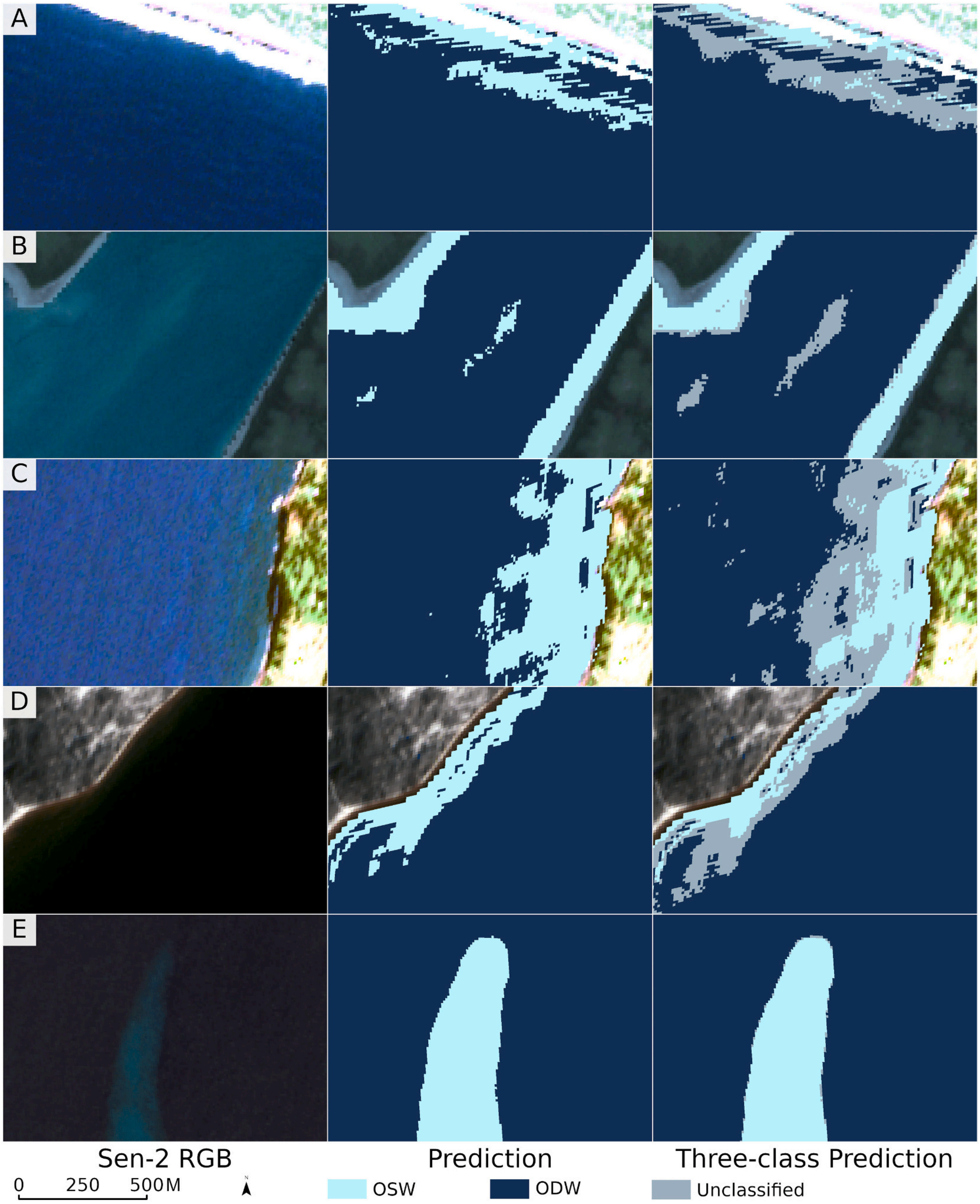

Fig. A.2. Zoomed-in version of the scenes presented in Fig. A.1 (left column), with binary predictions (middle column), and three-class predictions (right column) including an unclassified class defined using a probability threshold from 0.4 to 0.6, from the R_{WL} (A, B) and R_{TOA} (C, D, E) DNN models.

References

Abdolrasol, M.G.M., Hussain, S.M.S., Ustun, T.S., Sarker, M.R., Hannan, M.A., Mohamed, R., Ali, J.A., Mekhilef, S., Milad, A., 2021. Artificial neural networks based optimization techniques: a review. Electronics 10 (21), 2689. https://doi.org/10.3390/electronics10212689.

Ahola, R., Chénier, R., Sagram, M., Horner, Bradley, 2020. The impact of sensors for satellite derived bathymetry within the Canadian Arctic. Geomatica 74, 46–64. https://doi.org/10.1139/geomat-2019-0022.

Al Najar, M., El Bennioui, Y., Thoumyre, G., Almar, R., Bergsma, E.W.J., Benshila, R., Delvit, J.-M., Wilson, D.G., 2022. A combined color and wave-based approach to satellite derived bathymetry using deep learning. Int. Arch. Photogramm. Remote. Sens. Spat. Inf. Sci. XLIII-B3-2022, 9–16. https://doi.org/10.5194/isprs-archives-XLIII-B3-2022-9-2022.

Altmann, A., Toloşi, L., Sander, O., Lengauer, T., 2010. Permutation importance: a corrected feature importance measure. Bioinformatics 26 (10), 1340–1347. https://doi.org/10.1093/bioinformatics/btq134.

Aptoula, E., Ariman, S., 2022. Chlorophyll-a retrieval from Sentinel-2 images using convolutional neural network regression. IEEE Geosci. Remote Sens. Lett. 19, 1–5. https://doi.org/10.1109/LGRS.2021.3070437.

Arabi, B., Salama, Mhd.S., van der Wal, D., Pitarch, J., Verhoef, W., 2020. The impact of sea bottom effects on the retrieval of water constituent concentrations from MERIS and OLCI images in shallow tidal waters supported by radiative transfer modeling. Remote Sens. Environ. 237, 111596 https://doi.org/10.1016/j.rse.2019.111596.

Barredo Arrieta, A., Díaz-Rodríguez, N., Del Ser, J., Bennetot, A., Tabik, S., Barbado, A., Garcia, S., Gil-Lopez, S., Molina, D., Benjamins, R., Chatila, R., Herrera, F., 2020. Explainable artificial intelligence (XAI): concepts, taxonomies, opportunities and challenges toward responsible AI. Inform. Fusion 58, 82–115 doi: 10.1016/j.inffus.2019.12.012.

Bäuerle, A., van Onzenoodt, C., Ropinski, T., 2021. Net2Vis—a visual grammar for automatically generating publication-tailored CNN architecture visualizations. IEEE Trans. Vis. Comput. Graph. 27 (6), 2980–2991. https://doi.org/10.1109/TVCG.2021.3057483.

Bauer-Marschallinger, B., Falkner, K., 2023. Wasting petabytes: A survey of the Sentinel-2 UTM tiling grid and its spatial overhead. ISPRS J. Photogramm. Remote Sens. 202, 682–690. https://doi.org/10.1016/j.isprsjprs.2023.07.015.

Behnamian, A., Millard, K., Banks, S.N., White, L., Richardson, M., Pasher, J., 2017. A systematic approach for variable selection with random forests: achieving stable variable importance values. IEEE Geosci. Remote Sens. Lett. 14 (11), 1988–1992. https://doi.org/10.1109/LGRS.2017.2745049.

Brando, V.E., Anstee, J.M., Wettle, M., Dekker, A.G., Phinn, S.R., Roelfsema, C., 2009. A physics based retrieval and quality assessment of bathymetry from suboptimal hyperspectral data. Remote Sens. Environ. 113 (4), 755–770. https://doi.org/10.1016/j.rse.2008.12.003.

Breiman, L., 2001. Random forests. Mach. Learn. 45 (1), 5–32. https://doi.org/10.1023/A:1010933404324.

Breiman, L., Friedman, J., Olshen, R.A., Stone, C.J., 2017. Classification and regression trees. Routledge. https://doi.org/10.1201/9781315139470.

Burns, P., Nolin, A., 2014. Using atmospherically-corrected Landsat imagery to measure glacier area change in the cordillera Blanca, Peru from 1987 to 2010. Remote Sens. Environ. 140, 165–178. https://doi.org/10.1016/j.rse.2013.08.026.

Caballero, I., Stumpf, R.P., 2023. Confronting turbidity, the major challenge for satellite-derived coastal bathymetry. Sci. Total Environ. 870, 161898 https://doi.org/10.1016/j.scitotenv.2023.161898.

Champion, N., 2012. Automatic cloud detection from multi-temporal satellite images: towards the use of PLÉIADES time series. ISPRS - Int. Arch. Photogram. Remote Sens. Spatial Inform. Sci. 39B3, 559–564. https://doi.org/10.5194/isprsarchives-XXXIX-B3-559-2012.

Chen, T., Guestrin, C., 2016. XGBoost: A scalable tree boosting system. In: Proceedings of the 22nd ACM SIGKDD International Conference on Knowledge Discovery and Data Mining, pp. 785–794. https://doi.org/10.1145/2939672.2939785.

Chen, R.-C., Dewi, C., Huang, S.-W., Caraka, R.E., 2020. Selecting critical features for data classification based on machine learning methods. J. Big Data 7 (1), 52. https://doi.org/10.1186/s40537-020-00327-4.

Díaz-Uriarte, R., Alvarez de Andrés, S., 2006. Gene selection and classification of microarray data using random forest. BMC Bioinform. 7 (1), 3. https://doi.org/10.1186/1471-2105-7-3.

Díaz-Uriarte, R., de Andrés, S.A., 2004. Variable selection from random forests: application to gene expression data. In: Proceedings of the 5th Annual Spanish Bioinformatics Conference, pp. 47–52.

Eliason, S.R., 1993. Maximum Likelihood Estimation. SAGE Publications, Inc. https://doi.org/10.4135/9781412984928

ESA, 2024. MultiSpectral Instrument (MSI) Overview. Sentinel Online. https://copernicus.eu/technical-guides/sentinel-2-msi/msi-instrument.

Fawcett, T., 2006. An introduction to ROC analysis. Pattern Recogn. Lett. 27 (8), 861–874. https://doi.org/10.1016/j.patrec.2005.10.010.

Foga, S., Scaramuzza, P.L., Guo, S., Zhu, Z., Dilley, R.D., Beckmann, T., Schmidt, G.L., Dwyer, J.L., Joseph Hughes, M., Laue, B., 2017. Cloud detection algorithm comparison and validation for operational Landsat data products. Remote Sens. Environ. 194, 379–390. https://doi.org/10.1016/j.rse.2017.03.026.

Freund, Y., Schapire, R.E., 1997. A decision-theoretic generalization of on-line learning and an application to boosting. J. Comput. Syst. Sci. 55 (1), 119–139. https://doi.org/10.1006/jcss.1997.1504.

Friedman, J.H., 2001. Greedy function approximation: a gradient boosting machine. Ann. Stat. 29 (5), 1189–1232.

Genuer, R., Poggi, J.-M., Tuleau-Malot, C., 2010. Variable selection using random forests. Pattern Recogn. Lett. 31 (14), 2225–2236. https://doi.org/10.1016/j.patrec.2010.03.014.

Geurts, P., Ernst, D., Wehenkel, L., 2006. Extremely randomized trees. Mach. Learn. 63 (1), 3–42. https://doi.org/10.1007/s10994-006-6226-1.

Ghorbani, A., Abid, A., Zou, J., 2019. Interpretation of neural networks is fragile. Proc. AAAI Conf. Artific. Intell. 33 (01), 3681–3688. https://doi.org/10.1609/aaai.v33i01.33013681.

Hamylton, S.M., Hedley, J.D., Beaman, R.J., 2015. Derivation of high-resolution bathymetry from multispectral satellite imagery: a comparison of empirical and optimisation methods through geographical error analysis. Remote Sens. 7 (12) https://doi.org/10.3390/rs71215829. Article 12.

Harmel, T., Chami, M., Tormos, T., Reynaud, N., Danis, P.-A., 2018. Sunglint correction of the multi-spectral instrument (MSI)-SENTINEL-2 imagery over inland and sea waters from SWIR bands. Remote Sens. Environ. 204, 308–321. https://doi.org/10.1016/j.rse.2017.10.022.

Hasanin, T., Khoshgoftaar, T., 2018. The effects of random undersampling with simulated class imbalance for big data. In: 2018 IEEE International Conference on Information Reuse and Integration (IRI), pp. 70–79. https://doi.org/10.1109/IRI.2018.00018.

Hedley, J., Roelfsema, C., Koetz, B., Phinn, S., 2012. Capability of the sentinel 2 mission for tropical coral reef mapping and coral bleaching detection. Remote Sens. Environ. 120, 145–155. https://doi.org/10.1016/j.rse.2011.06.028.

Ho, J.C., Michalak, A.M., Pahlevan, N., 2019. Widespread global increase in intense lake phytoplankton blooms since the 1980s. Nature 574 (7780). https://doi.org/10.1038/s41586-019-1648-7. Article 7780.

Ilori, C.O., Pahlevan, N., Knudby, A., 2019. Analyzing performances of different atmospheric correction techniques for Landsat 8: application for coastal remote sensing. Remote Sens. 11 (4) https://doi.org/10.3390/rs11040469. Article 4.

Kelso, N.V., 2022. 10 m physical vectors [shapefile]. https://www.naturalearthdata.com/downloads/10m-physical-vectors/10m-coastline/.

Kingma, D.P., Ba, J., 2017. Adam: A Method for Stochastic Optimization (arXiv:1412.6980). arXiv. Doi: 10.48550/arXiv.1412.6980.

Knudby, A., Richardson, G., 2023. Incorporation of neighborhood information improves performance of SDB models. Remote Sens. Appl. Soc. Environ. 32, 101033 https://doi.org/10.1016/j.rsase.2023.101033.

Knudby, A., Nordlund, L.M., Palmqvist, G., Wikström, K., Koliji, A., Lindborg, R., Gullström, M., 2014. Using multiple Landsat scenes in an ensemble classifier reduces classification error in a stable nearshore environment. Int. J. Appl. Earth Obs. Geoinf. 28, 90–101.

Knudby, A., Ahmad, S.K., Ilori, C., 2016. The potential for Landsat-based bathymetry in Canada. Can. J. Remote. Sens. 42 (4), 367–378. https://doi.org/10.1080/07038992.2016.1177452.

Kwon, S., Shin, J., Seo, I.W., Noh, H., Jung, S.H., You, H., 2022. Measurement of suspended sediment concentration in open channel flows based on hyperspectral imagery from UAVs. Adv. Water Resour. 159, 104076 https://doi.org/10.1016/j.advwatres.2021.104076.

Lachenbruch, P.A., 2014. McNemar Test. In: Wiley StatsRef: Statistics Reference Online. John Wiley & Sons, Ltd. https://doi.org/10.1002/9781118445112.stat04876.

Lai, W., Lee, Z., Wang, J., Wang, Y., Garcia, R., Zhang, H., 2022. A portable algorithm to retrieve bottom depth of optically shallow waters from top-of-atmosphere measurements. J. Remote Sens. 2022, 16. https://doi.org/10.34133/2022/9831947.

Lee, Z., Shangguan, M., Garcia, R.A., Lai, W., Lu, X., Wang, J., Yan, X., 2021. Confidence measure of the shallow-water bathymetry map obtained through the fusion of Lidar and multiband image data. J. Remote Sens. 2021 https://doi.org/10.34133/2021/9841804.

Lee, C.B., Traganos, D., Reinartz, P., 2022. A simple cloud-native spectral transformation method to disentangle optically shallow and deep waters in Sentinel-2 images. Remote Sens. 14 (3) https://doi.org/10.3390/rs14030590. Article 3.

Lerman, P.M., 1980. Fitting segmented regression models by grid search. J. R. Stat. Soc.: Ser. C: Appl. Stat. 29 (1), 77–84. https://doi.org/10.2307/2346413.

Li, J., Knapp, D.E., Lyons, M., Roelfsema, C., Phinn, S., Schill, S.R., Asner, G.P., 2021. Automated global shallow water bathymetry mapping using Google Earth Engine. Remote Sens. 13 (8) https://doi.org/10.3390/rs13081469. Article 8.

Li, H., Li, X., Song, D., Nie, J., Liang, S., 2024. Prediction on daily spatial distribution of chlorophyll-a in coastal seas using a synthetic method of remote sensing, machine learning and numerical modeling. Sci. Total Environ. 910, 168642 https://doi.org/10.1016/j.scitotenv.2023.168642.

Liu, H., Li, Q., Bai, Y., Yang, C., Wang, J., Zhou, Q., Hu, S., Shi, T., Liao, X., Wu, G., 2021. Improving satellite retrieval of oceanic particulate organic carbon concentrations using machine learning methods. Remote Sens. Environ. 256, 112316 https://doi.org/10.1016/j.rse.2021.112316.

Ma, Y., Chen, S., Ermon, S., Lobell, D.B., 2024. Transfer learning in environmental remote sensing. Remote Sens. Environ. 301, 113924 https://doi.org/10.1016/j.rse.2023.113924.

Maxwell, A.E., Warner, T.A., Fang, F., 2018. Implementation of machine-learning classification in remote sensing: an applied review. Int. J. Remote Sens. 39 (9), 2784–2817. https://doi.org/10.1080/01431161.2018.1433343.

McFeeters, S.K., 1996. The use of the normalized difference water index (NDWI) in the delineation of open water features. Int. J. Remote Sens. 17 (7), 1425–1432. https://doi.org/10.1080/01431169608948714.

Myung, I.J., 2003. Tutorial on maximum likelihood estimation. J. Math. Psychol. 47 (1), 90–100. https://doi.org/10.1016/S0022-2496(02)00028-7.

Natekin, A., Knoll, A., 2013. Gradient boosting machines, a tutorial. Front. Neurorobot. 7 https://www.frontiersin.org/articles/10.3389/fnbot.2013.00021.

Nazari, F., Yan, W., 2021. Convolutional versus dense neural networks: Comparing the two neural networks' performance in predicting building operational energy use based on the building shape, 17, pp. 495–502. https://doi.org/10.26868/25222708.2021.30735.

Pahlevan, N., Lee, Z., Wei, J., Schaaf, C.B., Schott, J.R., Berk, A., 2014. On-orbit radiometric characterization of OLI (Landsat-8) for applications in aquatic remote sensing. Remote Sens. Environ. 154, 272–284. https://doi.org/10.1016/j.rse.2014.08.001.

Pahlevan, N., Chittimalli, S.K., Balasubramanian, S.V., Vellucci, V., 2019. Sentinel-2/Landsat-8 product consistency and implications for monitoring aquatic systems. Remote Sens. Environ. 220, 19–29. https://doi.org/10.1016/j.rse.2018.10.027.

Pahlevan, N., Mangin, A., Balasubramanian, S.V., Smith, B., Alikas, K., Arai, K., Barbosa, C., Bélanger, S., Binding, C., Bresciani, M., Giardino, C., Gurlin, D., Fan, Y., Harmel, T., Hunter, P., Ishikaza, J., Kratzer, S., Lehmann, M.K., Ligi, M., Warren, M., 2021. ACIX-aqua: a global assessment of atmospheric correction methods for Landsat-8 and Sentinel-2 over lakes, rivers, and coastal waters. Remote Sens. Environ. 258, 112366 https://doi.org/10.1016/j.rse.2021.112366.

Pedregosa, F., Varoquaux, G., Gramfort, A., Michel, V., Thirion, B., Grisel, O., Blondel, M., Prettenhofer, P., Weiss, R., Dubourg, V., Vanderplas, J., Passos, A., Cournapeau, D., Brucher, M., Perrot, M., Duchesnay, É., 2011. Scikit-learn: machine learning in Python. J. Mach. Learn. Res. 12 (85), 2825–2830.

Pembury Smith, M.Q.R., Ruxton, G.D., 2020. Effective use of the McNemar test. Behav. Ecol. Sociobiol. 74 (11), 133. https://doi.org/10.1007/s00265-020-02916-y.

Prusa, J., Khoshgoftaar, T.M., Dittman, D.J., Napolitano, A., 2015. Using random undersampling to alleviate class imbalance on tweet sentiment data. In: 2015 IEEE International Conference on Information Reuse and Integration, pp. 197–202. https://doi.org/10.1109/IRI.2015.39.

Rezaei, H., Sabokrou, M., 2023. Quantifying Overfitting: Evaluating Neural Network Performance through Analysis of Null Space (arXiv:2305.19424). arXiv. Doi: 10.48550/arXiv.2305.19424.

Richardson, G., Knudby, A., Chen, W., 2023a. Utilizing transfer learning with artificial intelligence for scaling-up lichen coverage maps. In: IGARSS 2023–2023 IEEE International Geoscience and Remote Sensing Symposium, 3050–3053. https://doi.org/10.1109/IGARSS52108.2023.10283197.

Richardson, G., Knudby, A., Chen, W., Sawada, M., Lovitt, J., He, L., Naeni, L.Y., 2023b. Dense neural network outperforms other machine learning models for scaling-up lichen cover maps in eastern Canada. PLoS One 18 (11), e0292839. https://doi.org/10.1371/journal.pone.0292839.

Ripley, B.D., 1996, January. Pattern Recognition and Neural Networks. Cambridge University Press, Cambridge Core. https://doi.org/10.1017/CBO9780511812651.

Salman, S., Liu, X., 2019. Overfitting Mechanism and Avoidance in Deep Neural Networks (arXiv:1901.06566). arXiv. doi: 10.48550/arXiv.1901.06566.

Schapire, R.E., 2003. The boosting approach to machine learning: An overview. In: Denison, D.D., Hansen, M.H., Holmes, C.C., Mallick, B., Yu, B. (Eds.), Nonlinear Estimation and Classification. Springer, pp. 149–171. https://doi.org/10.1007/978-0-387-21579-2_9.

Schapire, R.E., Freund, Y., 2012. Boosting: Foundations and Algorithms. MIT Press. http://ebookcentral.proquest.com/lib/ottawa/detail.action?docID=3339451.

Seabold, S., Perktold, J., 2010. Statsmodels: econometric and statistical modeling with Python. In: Proceedings of the 9th Python in Science Conference, pp. 92–96.

Sharr, M.B., Parrish, C.E., Jung, J., 2024. Automated classification of valid and invalid satellite derived bathymetry with random forest. Int. J. Appl. Earth Obs. Geoinf. 129, 103796 https://doi.org/10.1016/j.jag.2024.103796.

Shi, X., Gu, L., Li, X., Jiang, T., Gao, T., 2024. Automated spectral transfer learning strategy for semi-supervised regression on chlorophyll-a retrievals with Sentinel-2 imagery. Int. J. Digital Earth 17 (1), 2313856. https://doi.org/10.1080/17538947.2024.2313856.

Strahler, A.H., 1980. The use of prior probabilities in maximum likelihood classification of remotely sensed data. Remote Sens. Environ. 10 (2), 135–163. https://doi.org/10.1016/0034-4257(80)90011-5.

Tang, H., Yu, K., Hagolle, O., Jiang, K., Geng, X., Zhao, Y., 2013. A cloud detection method based on a time series of MODIS surface reflectance images. Int. J. Digital Earth 6 (sup1), 157–171. https://doi.org/10.1080/17538947.2013.833313.

van der Laan, M.J., Polley, E.C., Hubbard, A.E., 2007. Super learner. Stat. Appl. Genet. Mol. Biol. 6 (1) https://doi.org/10.2202/1544-6115.1309.

Vanhellemont, Q., 2019. Adaptation of the dark spectrum fitting atmospheric correction for aquatic applications of the Landsat and Sentinel-2 archives. Remote Sens. Environ. 225, 175–192. https://doi.org/10.1016/j.rse.2019.03.010.

Vanhellemont, Q., 2023. ACOLITE 20231023.0 manual. In: Royal Belgian Institute of Natural Sciences. https://github.com/acolite/acolite/releases/tag/20231023.0.

Vanhellemont, Q., Ruddick, K., 2018. Atmospheric correction of metre-scale optical satellite data for inland and coastal water applications. Remote Sens. Environ. 216, 586–597. https://doi.org/10.1016/j.rse.2018.07.015.

Wolpert, D.H., 1992. STACKED GENERALIZATION. Neural Netw. 5 (2), 241–259. https://doi.org/10.1016/S0893-6080(05)80023-1.

Zhong, L., Hu, L., Zhou, H., 2019. Deep learning based multi-temporal crop classification. Remote Sens. Environ. 221, 430–443. https://doi.org/10.1016/j.rse.2018.11.032.

Zhong, J., Sun, J., Lai, Z., Song, Y., 2022. Nearshore bathymetry from ICESat-2 LiDAR and Sentinel-2 imagery datasets using deep learning approach. Remote Sens. 14 (17) https://doi.org/10.3390/rs14174229. Article 17.